CELL BIOLOGY

Differential H4K16ac levels ensure a balance between quiescence and activation in hematopoietic stem cells

Cecilia Pessoa Rodrigues[1,2,3] and Asifa Akhtar[1]*

Hematopoietic stem cells (HSCs) are able to reconstitute the bone marrow while retaining their self-renewal property. Individual HSCs demonstrate heterogeneity in their repopulating capacities. Here, we found that the levels of the histone acetyltransferase MOF (males absent on the first) and its target modification histone H4 lysine 16 acetylation are heterogeneous among HSCs and influence their proliferation capacities. The increased proliferative capacities of MOF-depleted cells are linked to their expression of CD93. The CD93$^+$ HSC subpopulation simultaneously shows transcriptional features of quiescent HSCs and functional features of active HSCs. CD93$^+$ HSCs were expanded and exhibited an enhanced proliferative advantage in *Mof*$^{+/-}$ animals reminiscent of a premalignant state. Accordingly, low *MOF* and high *CD93* levels correlate with poor survival and increased proliferation capacity in leukemia. Collectively, our study indicates H4K16ac as an important determinant for HSC heterogeneity, which is linked to the onset of monocytic disorders.

INTRODUCTION

Hematopoietic stem cells (HSCs) are characterized by their ability to give rise to virtually all blood cell types while retaining their self-renewal capacity. Functionally, HSCs can repopulate and sustain multilineage engraftment even upon serial transplants into irradiated mice (*1*).

Single-cell HSC transplants, single-cell RNA sequencing (scRNA-seq), and high-throughput fluorescence-activated cell sorting (FACS) experiments revealed that multiple subtypes exist within the HSC compartment. Those subtypes can have different functional properties, including differences in repopulation kinetics (*2*–*5*), cell cycle status (*6*), self-renewal abilities (*7*), and multilineage differentiation output (*8*, *9*). However, the molecular factors giving rise to HSC heterogeneity and the functional consequences of this heterogeneity remain unclear.

Cell-extrinsic factors, mainly provided by the bone marrow microenvironment or niche, have long been suspected as the culprits for HSC heterogeneity (*10*). However, it has become apparent that the niche is not the only factor promoting HSC heterogeneity since single-cell HSC transplantation revealed that cells could undergo 1 of 16 different types of kinetic repopulation patterns once transplanted into the host, despite all other factors (including the niche) being stable in recipient mice (*3*, *4*).

These experiments suggest that cell-autonomous factors have a strong influence on HSC heterogeneity. In this sense, it is plausible that individual cells within the founder HSC population make independent cell-intrinsic decisions that are subsequently remembered by their daughter cells after they divide. Epigenetic modifications are likely to play a pivotal role in conveying this cell-intrinsic molecular memory, governing HSC heterogeneity and dynamics. Multiple epigenetic mechanisms have been shown to be involved in HSC maintenance, lineage commitment, aging, and malignant transformation (*11*–*13*). Those include the histone modifications H4 lysine 16 acetylation (H4K16ac) (*14*–*17*), H2A119Ub1 (*18*, *19*), H3K27me3 (*20*, *21*), H3K4me1/me2/me3 (*22*–*26*), and DNA methylation (*11*, *27*–*30*). Likewise, the chromatin landscape has been shown to be capable of instructing and reinforcing lineage-specific gene expression programs (*31*–*33*). The contribution of epigenetic factors to HSC heterogeneity is supported by in vivo clonal tracking approaches, showing a link between clone-specific epigenetic programs and distinct functional outcomes (*34*, *35*).

MOF (males absent on the first; also known as KAT8 or MYST1) is a lysine acetyltransferase (KAT) responsible for bulk histone H4K16ac (*36*). Chromatin regions marked by H4K16ac exhibit increased accessibility and therefore represent a more transcriptionally permissive state. Furthermore, previous studies have suggested that cells are exquisitely sensitive to levels of H4K16ac, with subtly different phenotypes emerging depending on the extent of MOF depletion (*37*). This chromatin modification is not only intergenerationally maintained but can also be passed to daughter cells through mitotic divisions (*38*). These unique properties of H4K16ac raise interesting questions about the possibility of this modification contributing to generating and maintaining HSC heterogeneity. The importance of MOF in HSC function is already established. Recent studies demonstrated that *Mof*-depleted HSCs cannot maintain adult hematopoiesis, resulting in decreased survival of adult mice due to severe anemia (*37*, *39*). Furthermore, *Mof*-depleted HSCs failed to sustain serial transplantations (*37*), suggesting that these cells might exhibit decreased self-renewal capacity upon severe stress. On the other hand, *MOF* down-regulation is a hallmark of acute myeloid leukemia (AML) in humans (*40*), suggesting that the observed self-renewal deficiency might be a consequence of enhanced proliferation capacity. *Mof*$^{+/-}$ mice show the accumulation of an otherwise rare HSC population (*37*). However, the influence of MOF in regulating HSC dynamics and heterogeneity need to be further investigated. In this study, we set out to investigate the possible contribution of H4K16ac to establishing HSC heterogeneity and propagating this to derived daughter cells of the hematopoietic lineage.

Here, we identify MOF as an important regulator of HSC quiescence and that inherent variability in H4K16ac levels promotes HSC heterogeneity. We identify that reduction of MOF levels leads

[1]Department of Chromatin Regulation, Max Planck Institute of Immunobiology and Epigenetics, 79108 Freiburg, Germany. [2]Faculty of Biology, University of Freiburg, Schaenzlestrasse 1, 79104 Freiburg, Germany. [3]International Max Planck Research School for Molecular and Cellular Biology (IMPRS-MCB), Freiburg, Germany.
*Corresponding author. Email: akhtar@ie-freiburg.mpg.de

to the expansion of an HSC subpopulation that expresses the membrane marker CD93. Our characterization reveals that this population is positioned just at the exit from dormancy to activation along the HSC cell state continuum. Furthermore, we show that the increased proliferation capacity exhibited by cells found in this intermediate cellular state is fine-tuned by their H4K16ac levels.

RESULTS

Quiescent HSCs are characterized by high H4K16ac levels

Previous studies have shown that HSC lineage fate decisions are fine-tuned by H4K16ac (*37*, *39*). This led us to ask whether HSCs display any intrinsic variation in H4K16ac levels. To characterize the H4K16ac pattern in HSCs in situ, we performed immunostaining of tissue samples. While the H4K16ac staining exhibited a homogeneous distribution in cells of the spleen and dermis, in the bone, we found that HSCs ($Lin^-CD34^-CD48^-c\text{-}Kit^+$) display a remarkable H4K16ac heterogeneity in situ (Fig. 1A, fig. S1A, and movies S1 to S4). Moreover, FACS analysis confirmed that the HSC compartment ($LSK^+CD34^-Flt3^-CD48^-CD150^+$) shows differential H4K16ac levels (fig. S1, B to C). Next, to test whether MOF/H4K16ac levels influence HSC activation, we sorted LSK^+ cells from wild-type mice and subjected them to polyinosinic:polycytidylic acid (poly I:C) stimulation in vitro. LSK^+ cells treated with poly I:C showed a significant decrease in the proportion of MOF^+ cells, confirming a relationship between MOF levels and the ability of hematopoietic stem progenitor cells (HSPCs) to rapidly respond to stimuli (fig. S1D).

Next, we decided to exploit the intrinsic heterogeneity found in colony formation [colony-forming unit (CFU)] assays to explore the relationship between chromatin landscape and HSC proliferation under steady-state conditions. To this end, we sorted HSCs ($LSK^+CD34^-Flt3^-CD48^-CD150^+$) and cultured them for CFU assay. After 10 days, we evaluated the levels of MOF, H4K16ac, and assay for transposase-accessible chromatin with visualization (ATAC-see) signal from 85 single colonies. We observed that smaller colonies, presumably reflecting cells with low proliferation capacity, exhibit a strong positive correlation among MOF, H4K16ac, and increased chromatin accessibility (Fig. 1, B to E). Meanwhile, the bigger colonies showed stochastic correlative values between MOF and H4K16ac, accompanied by decreased ATAC-see signal (Fig. 1, D and E). This supports the existence of an intrinsic heterogeneity in H4K16ac levels in hematopoietic cells. Furthermore, given the link between a permissive chromatin state and proliferation rate, decreased levels of MOF and H4K16ac appear to be associated with increased proliferative capacity and activation in HSCs.

To better understand the in vivo consequences of altered H4K16ac levels on HSC dynamics, we compared wild-type (+/+) and *Mof* heterozygous (+/−) HSCs in several aspects. We opted to analyze $Mof^{+/-}$ animals because this model shows robust decrease in MOF and H4K16ac levels without the defects on bone marrow cellularity observed in the *Vav1*-iCre $Mof^{flox/flox}$ conditional knockout mice (*37*). First, we sorted LSK^+ cells from both genotypes and probed the levels of known cyclin-dependent kinase inhibitors. In line with the increased proliferation hypothesis, the mutant cells showed decreased levels of $p16^{INKA}$ and $p19^{INKD}$ (fig. S1E), suggesting that *Mof* levels might influence HSPC cell cycle dynamics. Then, to understand whether this phenotype was intrinsic to HSCs or multipotent progenitors (MPPs), we single-cell–sorted HSCs and MPPs (LSK^+CD34^+). Before sorting, the cells were labeled with carboxyfluorescein succinimidyl ester (CFSE). After 10 days in culture, we harvested the daughter cells, and their proliferation capacity was measured by the extent of CFSE dilution (*41*, *42*). In line with the poly I:C results (fig. S1D), $Mof^{+/-}$ HSCs showed an increased proliferation ratio (fig. S1F) and division index, while the MPP cells showed a similar proliferation ratio to wild-type cells (HSC, $Mof^{+/+}$: 0.81; HSC, $Mof^{+/-}$: 1.081; MPP, $Mof^{+/+}$: 1.179; and MPP, $Mof^{+/-}$: 1.51) (fig. S1F). This suggested that the proliferative advantage likely originates with the HSCs rather than MPPs. To further validate these results, we sorted the daughter cells from the HSC colonies based on their CFSE intensity to obtain cells with high CFSE levels, representing undivided cells and cells with low CFSE marking proliferative cells. As expected, $Mof^{+/-}$ proliferating cells ($CFSE^{-/low}$) showed increased levels of *Mki67* (fig. S1G), a known proliferation marker. $Mof^{+/-}$ noncycling cells ($CFSE^{high}$) also showed increased levels of *Mki67* (fig. S1G). This result suggests that a decrease in MOF levels might be sufficient to promote the exit of HSCs from quiescence.

HSC dynamics are altered in *Mof* haploinsufficient animals

Considering that HSCs' proliferation status can be indicative of their functionality, we sought to investigate whether the inherent heterogeneity observed in H4K16ac levels (Fig. 1, A to D, and fig. S1, A and B) was also coupled to heterogeneous subpopulations across the HSC spectrum. Furthermore, we were curious whether H4K16ac levels could be used to classify HSCs into functional subpopulations. To explore the HSC subpopulations present in the $Mof^{+/-}$ mice, we reanalyzed scRNA-seq data from sorted progenitor cells, i.e., megakaryocyte progenitor ($Lin^-Sca\text{-}1^-c\text{-}Kit^+CD150^+CD41^+$; $n = 48$ cells), granulocyte–macrophage progenitors (GMP) ($Lin^-Sca\text{-}1^-c\text{-}Kit^+CD41^-FcγRII/III^+$; $n = 24$ cells), pre-GMP ($Lin^-Sca\text{-}1^-c\text{-}Kit^+CD41^-FcγRII/III^-CD150^-CD105^-$; $n = 24$ cells), pre–CFU-E (erythroid CFU) ($Lin^-Sca\text{-}1^-c\text{-}Kit^+CD41^-FcγRII/III^-CD150^+CD105^+$; $n = 48$ cells), megakaryocyte–erythroid progenitors (MEP) ($Lin^-Sca\text{-}1^-c\text{-}Kit^+CD150^+CD41^-FcγRII/III^-CD105^-$; $n = 48$ cells), pre-MEP ($Lin^-Sca\text{-}1^-c\text{-}Kit^+CD41^-FcγRII/III^-CD150^+CD105^-$; $n = 48$ cells), pre-erythroid ($CD71^+Ter119^{low}$; $n = 48$ cells), myeloid progenitor ($c\text{-}Kit^{high}Sca\text{-}1^-$; $n = 768$ cells), early progenitor ($LSK^+Flt3^-CD34^-$; $n = 576$ cells), HSCs ($LSK^+CD150^+CD48^-$; $n = 792$ cells), LSK^{high} ($n = 864$ cells), and LSK^{low} ($n = 576$ cells) (Fig. 1, F and G; fig. S2, A to C; and Materials and Methods) [original scRNA-seq data from (*37*)]. After cell type identification (Fig. 1, G and H), we found the differential enrichment of certain HSC subtypes in $Mof^{+/-}$ animals (Fig. 1I). This observation was also reported in our previous analysis of this dataset (*37*). To investigate the dynamics of these distinct populations, we subseted the HSCs (Fig. 1J) and performed RaceID, followed by StemID and VarID (*43*, *44*). These analyses permitted us to identify rare cell types and pinpoint cellular transitions based on expression variability within HSC clusters (fig. S2, D to H). We confirmed the HSC signature by probing the expression of *MoLO* genes (fig. S2E), followed by HSC population characterization (fig. S2F). Overall, we observed two major cellular transitions: (i) clusters 1 to 2 (S_1-S_2), associated with more stem-like cells, and (ii) clusters 5 to 4 (S_5-S_4), related to a more active status (fig. S2, F and G). Consistently, the subpopulation of HSCs undergoing the S_5-S_4 transition was expanded in $Mof^{+/-}$ mice, particularly, in cluster 5 (Fig. 1, K and L, and fig. S2D).

We then focused on the S_5-S_4 transition by exploring their pseudotime ordering, i.e., cluster 8 (high transcription entropy), cluster 5

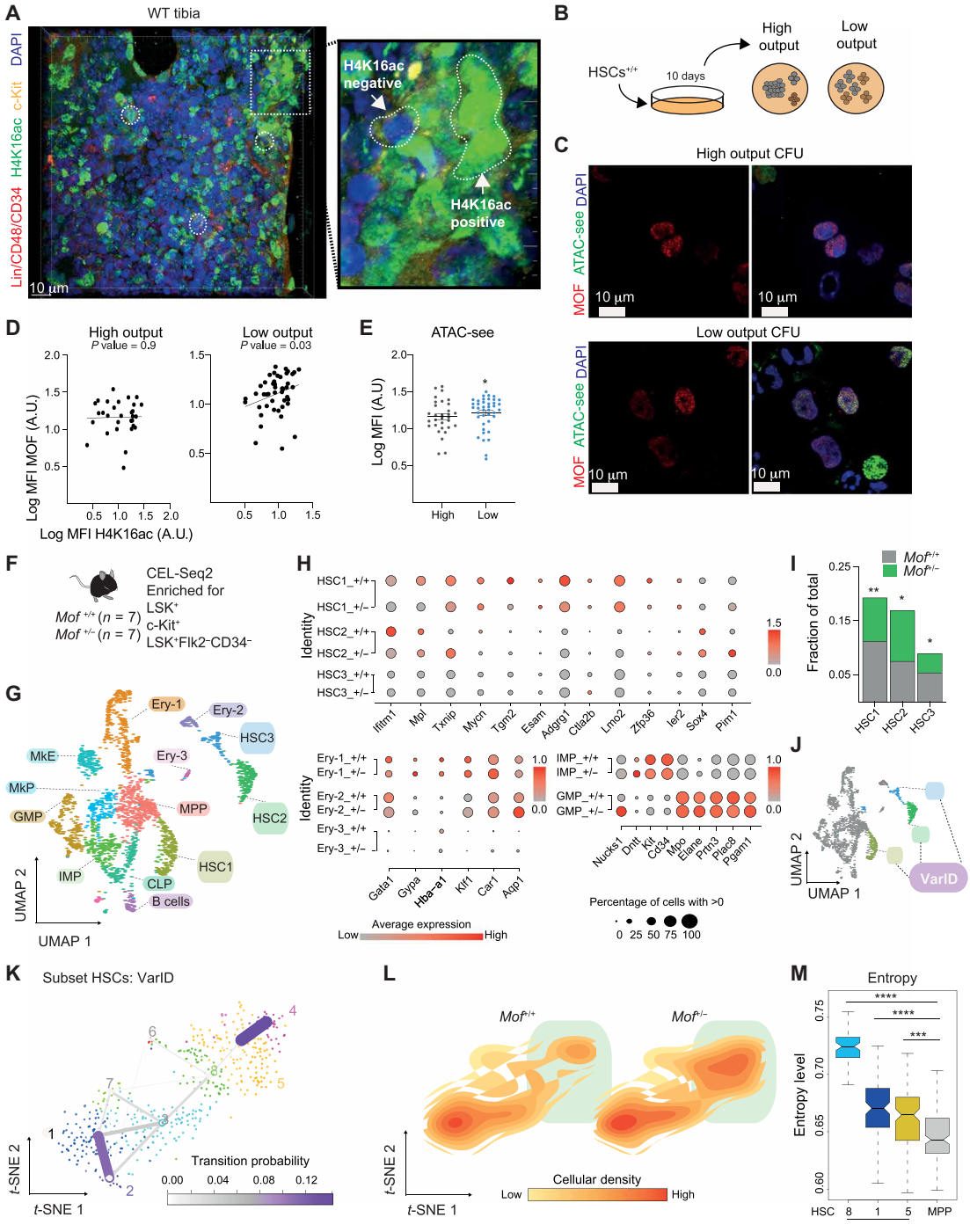

Fig. 1. Hematopoietic progenitor cells show heterogeneity in H4K16ac and MOF levels. (**A**) Tibia immunofluorescence (IF). Sections were stained with 4′,6-diamidino-2-phenylindole (DAPI) (blue), Lineage/CD34/CD48 (red), c-Kit (yellow), and H4K16ac (green). WT, wild type. (**B**) Scheme showing the colony formation [colony-forming unit (CFU)] stratification. (**C**) IF from high CFU and low CFU output. (**D**) Correlation between MOF and H4K16ac median fluorescence intensity (MFI) from both CFU outputs. Statistical value was determined by Pearson correlation and is indicated in the figure ($n = 4$ animals). A.U., arbitrary unit. (**E**) Chromatin accessibility from both CFU outputs. Significance was calculated using the t test. *$P = 0.05$. (**F**) scRNA-seq experiment design [original data from (*37*)]. (**G**) Uniform manifold approximation and projection (UMAP) of transcriptome similarities between each cell. (**H**) Expression of three major populations: HSC, erythroid (Ery), immature myeloid progenitors (IMP), and granulocyte/macrophage progenitors (GMP), all clusters inferred by Seurat. Genes queried for the populations were obtained from (*8*, *30*). (**I**) HSC subpopulation fraction for both genotypes. Statistical test was conducted using the Fisher test. *$P = 0.05$; **$P = 0.01$. (**J**) HSCs used for the StemID/VarID analysis (see fig. S2). (**K**) t-distributed stochastic neighbor embedding (t-SNE) with links connecting cluster medoids. The thickness and color of a link indicate the transition probability between the connected clusters. (**L**) Cellular density among the t-SNE for each genotype. The green square highlights the *Mof*$^{+/-}$ HSC enrichment. (**M**) Transcriptome entropy level for clusters 8, 1, and 5 from (K) and MPP from (G). Entropy was determined by FateID, and statistical significance was calculated by one-way analysis of variance (ANOVA) followed by Tukey post-test. ***$P < 0.001$ and ****$P < 0.0001$. The scRNA-seq data is from $n = 7$ biological replicates from two independent experiments.

(mid transcription entropy), and cluster 4 (low transcription entropy) (Fig. 1M and fig. S2G). Molecularly, cluster 5 cells were transcriptionally closer to the highest entropic HSC clusters (e.g., cluster 8), with concomitant expression of genes related to HSC activation, such as *Itga2* and *Cdk6* (Fig. 1M and fig. S2, G and H), suggesting that cluster 5 likely represents an intermediate cellular state between quiescent and active cells. Thus, to further understand this cellular transition, we compared both major identified cellular transitions, i.e., cluster 5 against clusters 1 and 2 (fig. S2I). As expected, cluster 5 showed a strong active signature in comparison to S_1-S_2 (fig. S2J). Cluster 5 displayed a strong HSC profile with a gradual decrease in expression of dormant markers, with a concomitant increase in expression of active HSC-related genes (fig. S2, F to K), thus supporting the notion that these cells acquire some features of activated HSCs while retaining features of quiescence. To better grasp the temporal location of cluster 5 cells, we performed pseudotime ordering from sorted dormant HSCs (dHSCs) and overall HSCs [original data from (*45*)]. Querying the expression of the significantly up-regulated genes in cluster 5 (table S1) along the pseudotime revealed that this cellular transition represents an intermediate state between dHSCs and more active cells (fig. S2, L to N), possibly akin to the "G_0-G_{alert}" stem cell population, which has the ability to actively and reversibly transition between the G_0 quiescent state and an active G_{alert} state in response to injury-induced systemic signals (*46*). Collectively, this finding suggests that cluster 5 represents an intermediate or primed HSC state across the HSC continuum.

CD93$^+$ HSCs are characterized by increased proliferative capacity

Studies of HSC dynamics are often hampered by two limiting factors: (i) the lack of a marker that is compatible with live cell sorting (*47*, *48*) and (ii) the lack of a marker that could be applied to human studies, since available methods for sorting viable HSCs typically rely on transgenic reporter mice, e.g., Gprc5c-GFP (green fluorescent protein) (*45*). Therefore, we asked whether the differentially variable genes marking the S_5-S_4 transition could be used to identify a cell population–specific cell surface marker (table S2) which is also conserved during evolution. We found *Cd93* as the best candidate because it is expressed in humans and was robustly and specifically expressed in cluster 5 (Fig. 2A and fig. S2F). Next, we performed FACS analysis to validate the existence of a CD93-expressing HSC population. We confirmed the existence of an HSC population that expresses CD93 on their membrane, as well as the expansion of this population in the *Mof*$^{+/-}$ animals (Fig. 2B).

To better understand the molecular characteristics of this HSC subpopulation, we sorted CD93$^+$ and CD93$^-$ HSCs (LSK$^+$CD34$^-$ Flt3$^-$CD48$^-$CD150$^+$) and performed bulk RNA-seq and Assay for Transposase-Accessible Chromatin using sequencing (ATAC-seq) analyses (fig. S3, A to D, and table S3). First, we evaluated the expression of HSC genes (*45*, *49*, *50*) and compared it to dHSCs, active HSCs (aHSCs), and MPP1 (*45*, *49*, *50*). This analysis revealed that, at the transcriptional level, CD93$^+$ HSCs showed a similar expression profile as the dHSCs (Fig. 2C). Concomitantly, we also found a significant positive correlation between the CD93$^+$ transcriptome and those of Tcf15$^+$ HSCs (quiescent cells), dHSCs, and multilineage cells (*8*, *45*). However, we found an unexpected negative correlation between RNAs expressed by CD93$^+$ cells and HSCs exhibiting enhanced self-renewal capacity (serially transplanted population), indicating that these cells are not in a canonical quiescent state (Fig. 2D) (*8*, *45*). Although, at first glance, the observed patterns seem discordant, the complex transcriptional phenotype exhibited by CD93$^+$ HSCs can be interpreted by their intermediate subtype identity. The unique characteristics of the CD93$^+$ population support the hypothesis that HSC activation does not occur in a binary manner but rather represents a continuum in which CD93$^+$ HSCs are likely at the edge of the quiescent state and primed to a more active state.

We next looked at the differences in expression profiles between the CD93$^+$ and the remaining CD93$^-$ populations. Unexpectedly, when compared to the pool of CD93$^-$ HSCs, most genes up-regulated in CD93$^+$ HSCs were associated with molecular signatures of HSC activation, notably cell cycle/mitosis, increased cell cycle capacity, DNA repair, and metabolism (Fig. 2, E and F; fig. S3B; and table S4). Besides decreased expression of genes associated with proliferation, CD93$^+$ HSCs also showed a reduction in genes related to cellular calcium homeostasis (Fig. 2F and table S4), a pathway that was recently shown to be required for maintenance of the dHSC state (*51*). Moreover, we found that CD93$^+$ HSCs show signs of increased mRNA splicing (Fig. 2G), which is an indicator of HSC activation (*45*). Together, these observations support the hypothesis that CD93$^+$ HSCs likely represents a primed HSC subtype.

To test whether CD93$^+$ HSCs were indeed primed, we evaluated their biological function in vitro. First, we evaluated their intrinsic proliferative capacity. To this end, we single-cell–sorted CD93$^-$ and CD93$^+$ HSCs, labeled them with CellTracker Red (CTR), and evaluated the dye dilution in the daughter cells after 10 days. In line with their RNA-seq profiles, CD93$^+$ HSCs showed higher proliferation indices after two generations, followed by a sharp decrease at the third generation, while CD93$^-$ cells displayed stable proliferation dynamics (Fig. 2H), thereby suggesting that the inverse transcriptional correlation with the serially transplanted cells we described earlier (Fig. 2D) might arise from the increased proliferative capacity of the CD93$^+$ HSCs. Consistently, CD93$^+$ HSCs also showed increased mitochondrial mass, reactive oxygen species (ROS), phosphorylated AKT-1 (p–AKT-1), and Ki67 (Fig. 2, I to L). These data suggested that CD93$^+$ cells are primed toward an active state and prone to respond faster due to their increased proliferation ratio (Fig. 2D).

Our data therefore support the idea that HSC activation does not take the form of a binary switch but rather represent a continuum in which CD93$^+$ HSCs are likely at the edge of the quiescent state and primed to a more active state. The CD93$^+$ population is much more abundant in *Mof*$^{+/-}$ HSCs relative to wild-type animals (Fig. 2B). CD93 therefore represents a molecular link between H4K16ac levels and maintenance of HSC quiescence.

High H4K16ac at target genes suppresses the CD93$^+$ HSCs' proliferative and in vitro self-renewal maintenance capacities

To investigate the role of MOF in regulating the quiescent to active transition, we first checked whether CD93$^+$ HSCs showed an overall decrease in *Mof* or H4K16ac (Fig. 3, A and B). We had previously demonstrated that *Mof*$^{+/-}$ mice harbor HSCs with significantly lowered H4K16ac across the population (*37*). Next, we asked whether MOF-bound regions in HSCs (*37*) were altered in CD93$^+$ HSCs. Thus, we overlapped the ATAC-seq profiles from CD93$^+$ or CD93$^-$ cells with MOF chromatin immunoprecipitation sequencing (ChIP-seq) targets. CD93$^+$ HSCs showed mild but significantly decreased

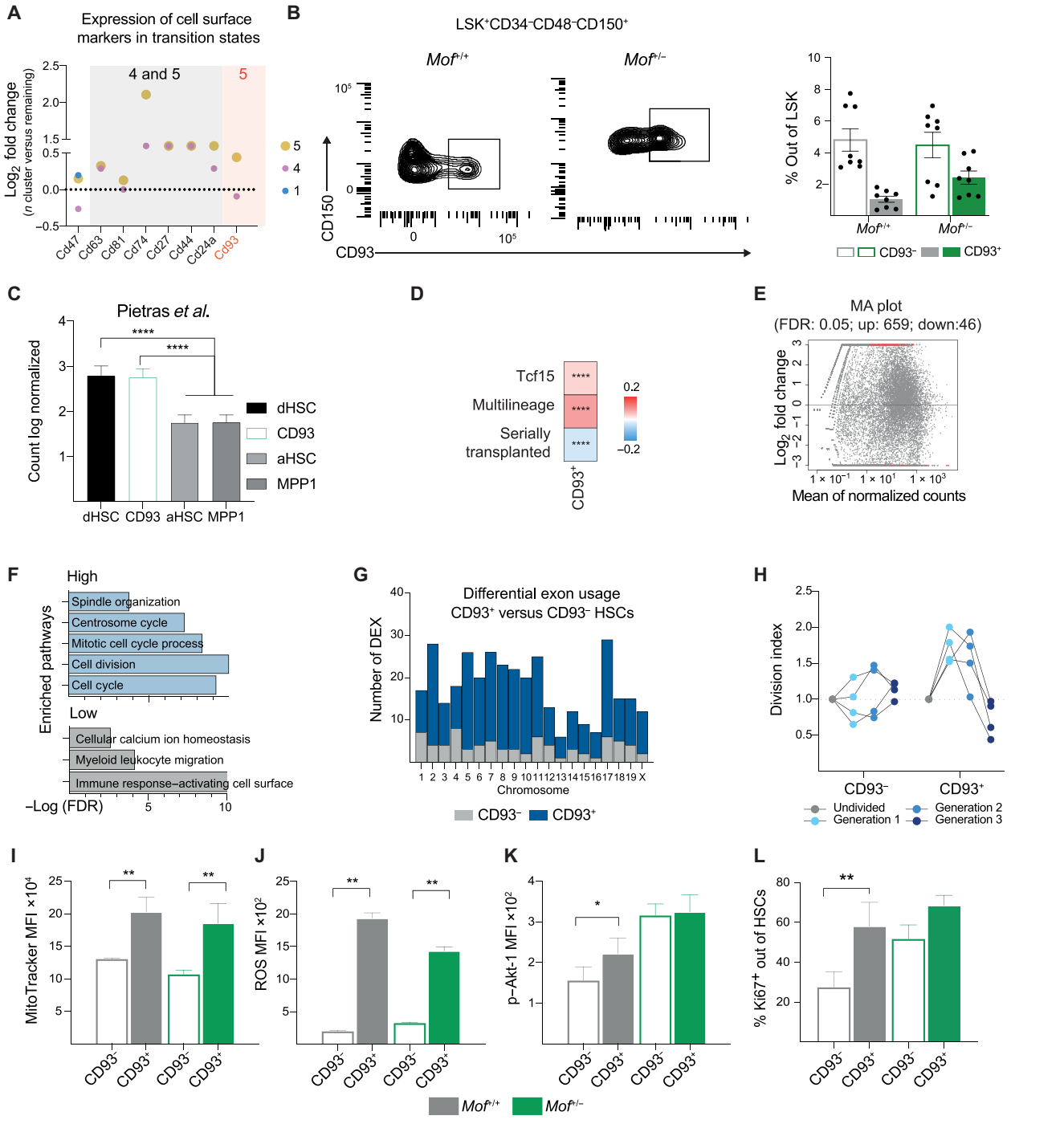

Fig. 2. CD93 expression identifies an intermediate HSC cellular state. (**A**) Expression of differentially variable cell surface markers in the S_5-S_4 transition. Colors indicate the clusters from Fig. 1K, cluster 5 (yellow), cluster 4 (magenta), and cluster 1 (blue). The orange rectangle indicates the specifically up-regulated marker defining cluster 5. (**B**) Contour plot showing the existence of CD93$^+$ HSCs. Bar plots showing the frequency out of LSK for the CD93$^+$ HSC population. Wild-type (gray) and *Mof*$^{+/-}$ (green). Empty bars show the CD93$^-$ HSC frequency and filled bars the CD93$^+$ frequency. (**C**) Log-normalized counts of HSC signature in dHSCs, CD93$^+$ HSCs, aHSCs, and MPP1 (*45*, *49*, *50*). Significance was determined by one-way ANOVA followed by Tukey post-test. ****$P < 0.001$. (**D**) Correlation map of the CD93$^+$ transcriptome against Tcf15$^+$ HSCs, HSCs that showed unbiased differentiation after transplantation (multilineage) and HSCs that had serial engrafted capacity (serially transplanted) [original data from (*8*)]. Colors indicate the *r* direction, positive correlation (red), and negative correlation (blue). Statistical value was determined by Spearman correlation test. ****$P < 0.001$. (**E**) Differentially regulated genes comparing CD93$^-$ versus CD93$^+$ HSCs. Red dots depict significantly regulated genes [false discovery rate (FDR) of 0.05]. (**F**) Enrichment pathway analysis for the up-regulated genes and down-regulated genes in CD93$^+$ HSCs. (**G**) Differential exon usage sequencing (DEX-seq) analysis for DEX in CD93$^-$ (gray) and CD93$^+$ (navy) HSCs. (**H**) Line plots showing the overall division index (proliferation index from *n* generation/proliferation index from undivided cells) for CD93$^-$ and CD93$^+$ HSC clones. (**I** to **L**) Biological characterization for active HSCs parameters: (I) mitochondrial mass ($n = 3$), (J) ROS ($n = 3$), (K) p–Akt-1 ($n = 6$) (K), and (L) Ki67$^+$ cell frequency ($n = 7$). Colors indicate the genotype. After normality test, *P* value was determined by one-way ANOVA followed by Holm-Sidak's test. *$P = 0.05$ and **$P = 0.01$.

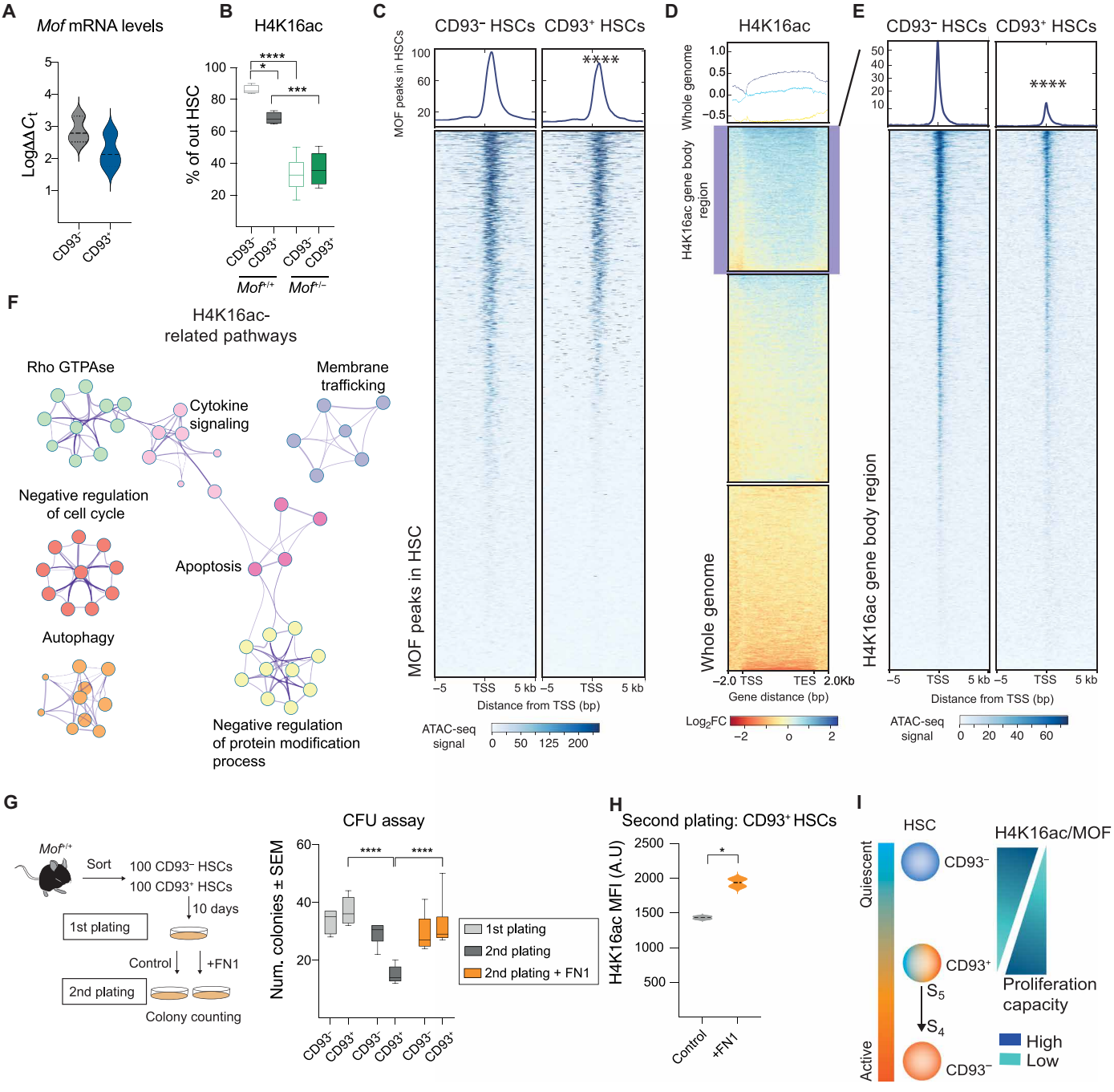

Fig. 3. Chromatin landscape characterization of CD93$^+$ HSCs. (**A**) Violin plot showing reverse transcription quantitative polymerase chain reaction (RT-qPCR) analyses of *Mof* levels in CD93$^-$ and CD93$^+$ HSCs isolated from wild-type animals. *Mof* expression was determined by [C_t-*Mof* – C_t-*Hprt*, ΔC_t] and then normalized by the smallest $^{\Delta}C_t$, $^{\Delta\Delta}C_t$. The log fold change is $2^{\Delta\Delta}C_t$ ($n = 3$). (**B**) H4K16ac levels in CD93$^-$ (empty boxes) and CD93$^+$ (filled boxes) from wild type (gray) and *Mof*$^{+/-}$ (green; $n = 4$ mice per genotype). Statistical significance was determined by one-way ANOVA followed by Tukey post-test. *$P = 0.05$; ***$P < 0.001$ and ****$P < 0.0001$. (**C**) Heatmap showing the enrichment of MOF target regions in HSCs (*37*) overlapped with the ATAC-seq profile from CD93$^-$ and CD93$^+$ HSCs. TES, transcription end site; TSS, transcription start site. ****$P < 0.0001$. (**D**) Heatmap showing the enrichment of H4K16ac over the entire mouse genome. (**E**) Heatmap showing the association of the stereotypical gene body regions from H4K16ac were selected and plotted against the CD93$^-$ and CD93$^+$ ATAC-seq profile. Statistical significance was determined by sampling the average scores for the genomic region of MOF targets (C) or H4K16ac gene body enriched (D) using the MultibigwigSummary() software. Score comparison was conducted by the nonparametric Mann-Whitney test. ****$P < 0.001$. (**F**) Network analysis showing the biological pathways related to H4K16ac enriched genes ($n = 2$). (**G**) Left: Serial CFU plating scheme. Right: Boxplot showing the total number of colonies in the first plating, second plating without FN1, or second plating with FN1 (100 μg/ml) ($n = 6$). Statistical analysis was determined by two-way ANOVA followed by Holm-Sidak multiple test. ****$P < 0.0001$. (**H**) H4K16ac levels upon FN1 treatment. Statistical analysis was determined by *t* test. *$P = 0.05$. ($n = 6$). (**I**) Graphical model showing the relation between H4K16ac levels and HSC activation status.

overall chromatin accessibility at MOF-bound regions (Fig. 3C). However, regions exhibiting high H4K16ac in the HPC7 hematopoietic progenitor cell line showed significant loss of chromatin accessibility in the CD93$^+$ cell population (Fig. 3, D and E). Furthermore, when we probed the molecular signatures of the MOF target genes that exhibited a loss of chromatin accessibility in CD93$^+$ cells, we found a significant enrichment for terms related to maintenance of HSC quiescence (Fig. 3F), including autophagy, negative regulation of protein modification, negative regulation of cell cycle, and Rho guanosine triphosphatase (GTPase). We also found that CD93$^+$ HSCs expressed higher cyclin-dependent kinase 6 (CDK6) protein levels (fig. S3E). We did not observe significant changes in other chromatin modifications, i.e., H3K27ac and H3K4me1 in long-term HSCs and HPC7 (fig. S3F) [original ChIP from (*32*, *52*)]. Moreover, no significant differences were observed in H4K5ac, H4K8ac, or H3K4me3 levels between CD93$^-$ and CD93$^+$ HSCs (fig. S3G), suggesting that H4K16ac is the main altered chromatin modification in CD93$^+$ HSCs. Our results indicate that MOF-mediated H4K16ac deposition is one of the main cell-intrinsic factors determining the unique gene expression profile of CD93$^+$ HSCs.

Next, we were interested in identifying niche signals that could influence H4K16ac levels in CD93$^+$ HSCs and, thereby, regulate their proliferation capacity. CD93 has previously been described as a receptor for the complement factor C1q, but these findings appear to be controversial (*53*–*56*). Recently, the extracellular matrix protein fibronectin (FN1) was shown to be a CD93 ligand (*57*). Given that HSCs treated with FN1 have increased self-renewal capacity (*58*), we asked whether FN1 could directly rescue CD93$^+$ HSC CFU colony formation and influence H4K16ac levels. To this end, we performed a serial plating experiment in which we sorted CD93$^-$ and CD93$^+$ HSCs and cultured them in methylcellulose complete media for 10 days. Then, we harvested the cells and plated 1000 daughter cells in a new well in the presence or absence of FN1. In line with our previous observations, we found that CD93$^+$ HSCs failed to sustain their colony formation capacity. However, FN1-treated CD93$^+$ HSCs showed a similar CFU capacity to the CD93$^-$ HSCs, while FN1-treated CD93$^-$ HSCs showed no significant differences to their untreated counterparts (Fig. 3G). Furthermore, daughter cells from CD93$^+$ HSCs treated with FN1 showed increased levels of H4K16ac (Fig. 3H), while FN1 did not rescue the *Mof*$^{+/-}$ HSCs' CFU capacity (fig. S4A). This suggests that FN1 acts as a stop signal, triggering CD93$^+$ HSCs to inhibit their proliferation program through elevated H4K16ac.

Since CD93 is also a marker for early B cells, a cell type known for their proliferative expansion capacities, we reanalyzed scRNA-seq data from FACS-sorted common lymphoid progenitors (CLPs; Lin$^-$Sca^{int} Kit^{int} Flt3$^+$), fraction A pre–pro-B cells (B220$^+$CD43$^+$ NK1.1$^-$BST2$^-$HSA$^-$BP1$^-$), and fraction B/C pro-B cells (B220$^+$ CD43$^+$NK1.1$^-$BST2$^-$HSA$^+$BP1$^+$) from wild-type mice (fig. S4B) (*43*, *59*). Next, we overlapped the significantly up-regulated genes in CD93$^+$ HSCs with the clusters representing the major developmental stages in B cell development (fig. S4C). We observed a significant overlap between CD93$^+$ HSCs and cycling pre–pro-B cells (fig. S4D). This suggests that the pathway through which CD93 modulates proliferation dynamics is common to both cell types. Collectively, our findings support the notion that HSC activation occurs in a continuum, wherein CD93$^+$ HSCs represent an intermediate cellular state and are primed to be active by their exquisitely fine-tuned H4K16ac levels (Fig. 3I).

CD93$^+$ HSCs respond faster to homeostatic insults

To investigate whether CD93$^+$ HSCs are able to respond faster in vivo, we treated wild-type and *Mof*$^{+/-}$ mice with five pulses of interferon-α (IFN-α), a cytokine known to disrupt HSC quiescence (*60*). After the treatment, the animals were injected with bromodeoxyuridine (BrdU). Seven days later, the animals were euthanized and the proliferation rates of their HSCs were evaluated (see Materials and Methods). In agreement with the in vitro results (Fig. 2, H to L), CD93$^+$ HSCs showed increased frequency of BrdU incorporation (Fig. 4A). This response was further enhanced by the *Mof*$^{+/-}$ background, suggesting that decreasing the levels of this enzyme removes the restraint on the existing proliferative tendencies of the CD93$^+$ HSC population.

To test whether *Mof*$^{+/-}$ HSCs indeed exhibit a proliferative advantage over wild-type cells, we performed in vitro cell competition assays. We sorted CD93$^-$ and CD93$^+$ HSCs from CD45.1 animals (wild type), the same set from CD45.2 animals (*Mof*$^{+/-}$), and cultured them together in a 1:1 ratio. After 10 days in culture, we evaluated the composition of the daughter cell populations (Fig. 4B). As expected from our BrdU labeling experiments, we observed a marked increase in proliferation in CD93$^+$ cells compared to their CD93$^-$ counterparts. Notably, reducing MOF levels (through *Mof* haploinsufficiency) conferred a significant proliferative advantage to both CD93$^+$ and CD93$^-$ HSC subtypes (Fig. 4, A and B), presumably due to their intrinsic decrease in H4K16ac levels.

Along with increased proliferation capacity, CD93$^+$ HSCs showed impaired serial plating capacity since they gave rise to fewer colonies upon serial plating (Fig. 4, C and D). This is associated with low numbers of remaining progenitor cells and decreased Ki67 staining (Fig. 4, E and F). On the other hand, *Mof*$^{+/-}$ HSCs showed similar numbers of colonies in the second plating and high numbers of proliferative progenitor cells (Fig. 4, E and F). These findings lead us to speculate that low levels of MOF might set the stage for later development of hematopoietic proliferative disorders.

Immune surveillance plays a critical role in regulating the numbers of CD93$^+$ HSCs in *Mof*$^{+/-}$ animals

Considering that *Mof*$^{+/-}$ animals have a normal life span and do not develop leukemia, we sought to explore the cell-cell interactions of CD93$^+$ HSCs with the immune system to test for a potential involvement of immune surveillance in blocking the onset of tumors. To this end, we took advantage of our scRNA-seq data and conducted ligand-receptor analysis using the immune checkpoint database. This analysis revealed that wild-type CD93$^+$ HSCs exhibit a strong predicted interaction with innate cells such as macrophages, dendritic cells (DCs), and neutrophils, while their *Mof*$^{+/-}$ counterparts showed weaker but numerous interactions with adaptive immune cells, including T and B cells (Fig. 5A). We additionally found increased frequencies of CD3$^+$ cells in the bone marrow, but not in the lymph nodes, of *Mof*$^{+/-}$ animals (Fig. 5B).

The increased frequency of their inferred cell-cell interaction in *Mof*$^{+/-}$ animals (Fig. 5A) led us to suspect that T cells may have a role in suppressing the proliferative potential of CD93$^+$ cells. T cells have a prominent role in hindering the onset of hematopoietic proliferative disorders (*61*). We crossed *Mof*$^{+/-}$ mice with *Rag-1* knockout animals (*Rag-1* KO), allowing us to study the consequences on CD93$^+$ HSCs in the absence of adaptive immune cells (Fig. 5C and fig. S5, A to D). We found that immune-deficient *Mof*$^{+/-}$ mice showed an augmented total frequency of CD93$^+$ HSCs in their bone

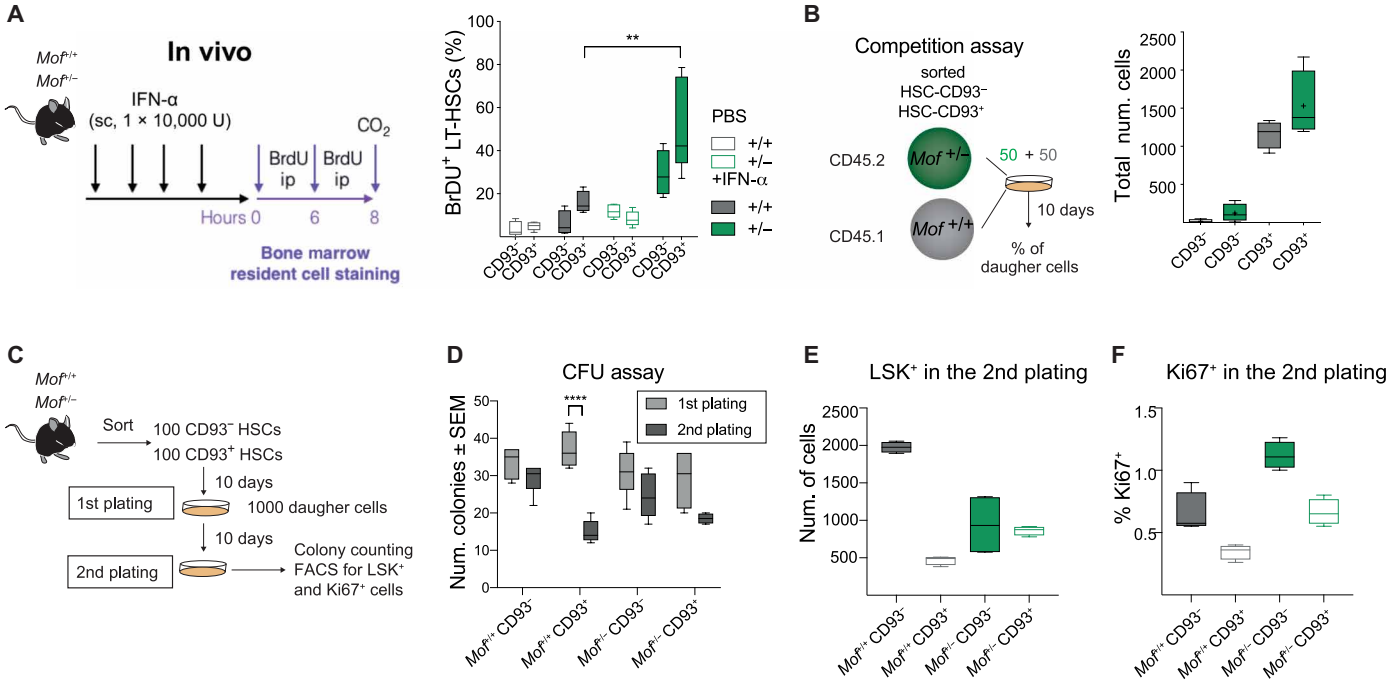

Fig. 4. Decreased levels of *Mof* confer a proliferative advantage to CD93$^+$ HSCs, leading to hematopoietic disorders when in the absence of adaptive immune cells. (**A**) Design of the BrdU incorporation upon IFN-α challenge. Right: Boxplots showing the frequency of BrdU-positive HSC ($n = 5$). Empty box represent the animals treated with PBS, and filled box represent animals treated with IFN-α. Colors indicate the genotype, wild type (gray) and *Mof*$^{+/-}$ (green). After the data normality test, statistical analysis was determined by one-way ANOVA followed by Tukey post-test. $^{**}P = 0.01$. ip, immunoprecipitation. (**B**) Graphic scheme showing the experimental design for the competition assay. *Mof*$^{+/-}$ HSCs (CD45.2$^+$) and wild-type HSCs (CD45.1$^+$) were cultured at a 1:1 ratio. After 10 days, cells were harvested, and daughter cells were evaluated for their ontogeny. Right: Boxplot showing the total of daughter cells. $n = 4$. (**C**) Graphical scheme showing the serial CFU assay design. (**D**) Boxplot showing the total number of colonies for first and second plating. After the normality test, statistical value was determined by one-way ANOVA followed by Tukey post-test. $^{****}P < 0.0001$ ($n = 4$). (**E**) Total number of LSK$^+$ cells from the second plating. (**F**) Frequency of Ki67$^+$ cells from the second plating.

marrow (Fig. 5, D and E) and a significant increase in circulating monocytes (Fig. 5F), despite the overall decrease in cellularity (fig. S5B). Both migratory and resident monocytes displayed increased levels of c-Kit (Fig. 5, G and H, and fig. S5A). We suspect that the increased frequency of interactions between CD93$^+$ HSCs and innate cells observed in our *Mof*$^{+/-}$ scRNA-seq are likely elicited by the organism in an attempt to contain the expansion of CD93$^+$ HSCs, which positively correlates with the appearance of immature circulating myeloid cells. Their increased proliferation and frequency of interaction with adaptive immune cells suggested that CD93$^+$ cells might increase the risk of developing hematopoietic proliferative disorders.

MOF as a potential target in the treatment of human leukemia

Aged HSCs have been shown to have intrinsically low H4K16ac levels (*14*, *15*, *62*); thus, we sought to investigate whether the status of CD93$^+$ HSCs in old animals was also altered. Aged animals (>60 weeks) exhibited a marked expansion of the CD93$^+$ HSC pool relative to young animals (<12 weeks), corroborating our findings that H4K16ac levels regulate the emergence of CD93$^+$ HSCs (Fig. 6A). We noticed that the *Cd93* locus showed increased signal in CD93$^+$ HSCs and in *Mof*$^{+/-}$ HSCs, which was associated with an accessible upstream region carrying a binding motif for the transcription factor ZFP128 (fig. S6A). These observations suggest that decrease of MOF facilitates transcription of the *Cd93* locus.

Considering that HSC aging is associated with increased prevalence of AML and clonal hematopoiesis of indeterminate potential (CHIP), we next reanalyzed published RNA-seq (*63*) from healthy HSCs (control), preleukemic stem cells (rHSCs), leukemic stem cells (LSCs), and blast cells (Blast). We found that *MOF* and *CD93* levels exhibit a gradient across the time scale of disease progression (Fig. 6, B and C), wherein low levels of *MOF* are observed in conjunction with increased levels in *CD93* in LSCs. This cell type represents the principal component (PC) critical point, showing ±48% of transcriptome differences related to HSCs and rHSCs (Fig. 6B), suggesting that decreased *MOF* levels are inversely correlated with transcriptome variability. Moreover, we found that LSCs displayed a significant decrease in the expression of human orthologs of mouse MOF HSC target genes (Fig. 6D), suggesting that the transcriptome of human LSCs is affected by *MOF* levels. Nevertheless, because of the small number of patients in this study, we reanalyzed the RNA-seq data from 437 healthy individuals and patients with AML [Leucegene, AML sequencing; original data from (*64*)]. On the basis of *MOF* and *CD93* expression, we could validate the existence of a group of patients with AML that have decreased levels of *MOF* but increased levels of *CD93* (Fig. 6E).

We were curious to explore whether *MOF* levels would affect disease outcome. We found that decreased levels of *MOF* are significantly associated with decreased survival probability in patients with AML (Fig. 6F and fig. S6, B and C) [original data from (*65*–*67*)]. We depleted *MOF* via knockdown (KD) in several leukemic cell

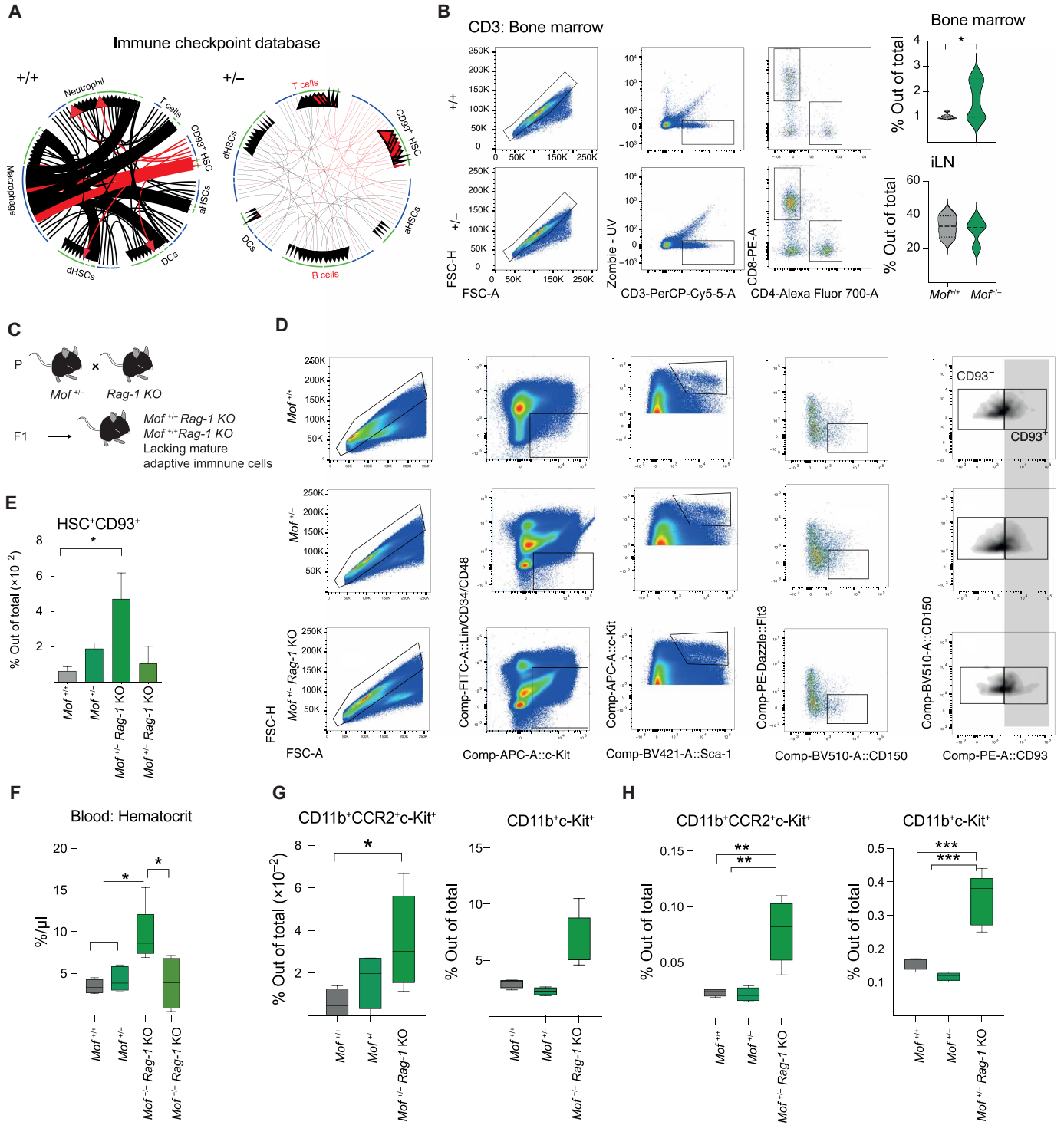

Fig. 5. T cells regulate the number of CD93$^+$ HSCs and hinder the onset of monocytic disorders. (**A**) Ligand-receptor circus plot from our scRNA-seq profile (Fig. 1). The immune checkpoint database was used to determine the interaction of progenitor cells and immune cells. Arrows indicate the cell interaction directionality. Thickness of the line depicts the interaction intensity. Red lines highlight the CD93$^+$ HSC interactions. (**B**) Left: Gating strategy showing the frequency of T cells in the bone marrow. Right: Quantification of CD3$^+$ in the bone marrow and inguinal lymph nodes (iLN). Statistical analysis was determined by *t* test. **P* = 0.05. (*n* = 4). (**C**) Graphic scheme showing the cross strategy to deplete the adaptive immune cell from *Mof*$^{+/–}$ animals. (**D**) Gating strategy showing the frequency of CD93$^+$ HSCs. (**E**) Total frequency of CD93$^+$ HSCs in wild-type (*n* = 14), *Mof*$^{+/–}$ (*n* = 11), *Mof*$^{+/–}$ *Rag-1* knockout (*Rag-1* KO) (*n* = 13), and *Rag-1* KO (*n* = 3). (**F**) Frequency of blood-circulating monocytes (wild type, *n* = 4; *Mof*$^{+/–}$, *n* = 5; *Mof*$^{+/–}$ *Rag-1* KO, *n* = 4). (**G**) Total frequency of immature migratory (CCR2$^+$) and CCR2$^–$ monocytes in the blood. (**H**) Total frequency of migratory (left) and tissue-resident (right) immature monocytes in spleen from wild type (*n* = 4), *Mof*$^{+/–}$ (*n* = 4), and *Mof*$^{+/–}$ *Rag-1* KO (*n* = 6). After the normality test, statistical value was determined by one-way ANOVA followed by Tukey post-test. **P* = 0.05, ***P* = 0.01 and ****P* < 0.001.

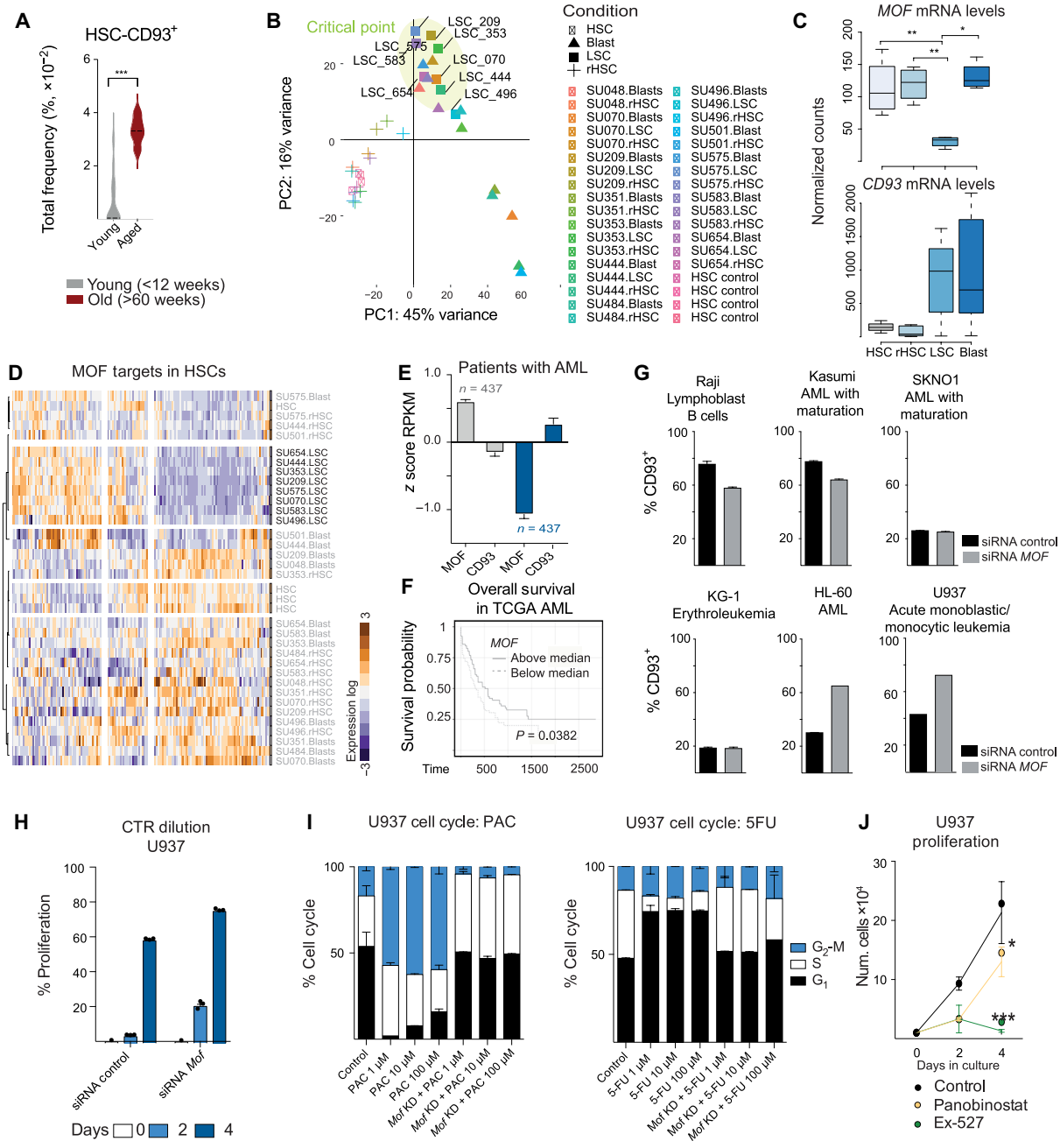

Fig. 6. *MOF* and *CD93* emerge as potential candidates to stratify human AML. (**A**) Violin plot showing the total frequency of HSC-CD93$^+$ in young (<12 weeks; $n = 14$) and aged (>60 weeks; $n = 5$) animals. Statistical significance was determined by Mann-Whitney test. ***$P < 0.001$. (**B**) Principal components analysis (PCA) plot showing the transcriptome variance of HSCs (healthy donor), rHCS (preleukemic HSCs), leukemic stem cells (LSCs), and blast cells. LSCs are highlighted in the plot as they represent the critical variable point. (**C**) DESeq2-normalized counts of *MOF* and *CD93* expression from (B). (**D**) Heatmap depicting the expression of the MOF target orthologs. The reference patient is indicated at the right side of the heatmap. LCSs are highlighted. Original data from (*63*). (**E**) Bar plots showing the *z* score reads per kilobase per million mapped reads (RPKM) of *MOF* and *CD93*. Data from GSE49642. (**F**) Kaplan-Meier plot showing the patients with AML survival probability in relation to *MOF* expression [original data from The Cancer Genome Atlas (TCGA)]. (**G**) Bar plots showing the total frequency of CD93$^+$ cells after *MOF* knockdown (KD). Steady state (black bar) or *MOF* KD cells (gray bar). The Orphanet (ORDO) definition is indicated underneath the cell line name. (**H**) Bar plots showing the CTR dilution of U937 after *Mof* KD (siRNA *Mof*). (**I**) Stack plot showing the cell cycle of U937 wild-type or *MOF* KD cells treated or not with PAC or 5-FU. (**J**) Line plot showing the number of cells of U937 cells after panobinostat (yellow line) and Ex-527 (green line). After the data normality test, the statistical value's significance was determined by two-way ANOVA. Data are from four independent experiments. *$P = 0.05$, **$P < 0.01$, and ***$P < 0.001$.

lines (fig. S5C). The monoblast U937 and myeloblast HL-60 lines (*68*) were the only ones among those tested showing increased proliferation and CD93 expression upon *MOF* KD (Fig. 6, G and H, and fig. S6, D to F). These results in human cells are consistent with the monocytic phenotype elicited by the depletion of adaptive immune cells in the $Mof^{+/-}$ mice (Fig. 3E).

To test whether *MOF* KD also confers protection to cell cycle blockers, we treated U937 cells subjected to *MOF* or scrambled KD with paclitaxel (PAC) that promotes microtubule stabilization, causing mitotic arrest, or with 5-fluorouracil (5-FU), known for inhibiting DNA synthesis by restricting availability of thymidylate. We found that *MOF* KD cells were less sensitive to these treatments, as we did not observe a decrease in the G_1 state (Fig. 6I), suggesting that low levels of *MOF* are sufficient to boost AML proliferation capacity.

We then asked whether the increased proliferation could be attenuated by reestablishment of H4K16ac levels. Therefore, we either overexpressed *Mof* or treated cells with Ex-547, a Sirtuin 1 (SIRT1) inhibitor that is selective toward H4K16ac (*37*, *69*), or the pan–histone deacetylase (HDAC) inhibitor panobinostat. In all treatment conditions, cells with augmented H4K16ac levels showed a decreased proliferation capacity (Fig. 6J and fig. S6G).

Together, our data revealed the existence of an AML patient subgroup that exhibits decreased levels of *MOF* concurrent with increased levels of *CD93*. At the cellular level, this leads to increased proliferation capacity that can be manipulated by H4K16ac levels, suggesting that drugs targeting MOF might be a good strategy against highly proliferative leukemic cells.

DISCUSSION

In this study, we characterize an intermediate HSC state marked by CD93 that resides in the bone marrow and is expanded in animals harboring low levels of H4K16ac. This HSC subset is transcriptionally akin to dormant HSCs but is primed toward activation. This allows $CD93^+$ HSCs to respond faster upon repopulation or cytokine exposure through increased proliferation but presumably at the expense of their self-renewal capacity. Furthermore, $CD93^+$ HSCs from $Mof^{+/-}$ animals showed a competitive proliferative advantage and appeared to maintain their progenitor pool to a certain extent. The combination of these properties could be deleterious in the AML context. In agreement, we identified a group of patients with AML showing low *MOF* and high *CD93* levels, which correlates with a poor survival presumably due to their increased proliferation capacity.

Our findings directly link HSC heterogeneity to epigenetic regulation. We observed that altered H4K16ac levels result in different HSC kinetics and varying degrees of accumulation of the $CD93^+$ population. This subpopulation emerged as an intermediate cellular state, displaying a compound phenotype consisting of high-transcription entropy levels and a robust dHSC molecular signature while harboring active features including increased mitochondrial mass, CDK6, and p–Akt-1 levels (*45*, *60*, *70*). Considering that HSC activation is linked to increased DNA damage, which over time might have consequences for the onset of hematopoietic disorders including CHIP and leukemia (*71*, *72*), we envisioned that the fast response of the $CD93^+$ HSCs might confer protection to the cells in the more dormant end of the HSC spectrum.

We found that $Mof^{+/-}$ animals have a higher frequency of $CD93^+$ cells. Although speculative, we hypothesize that the life-long anemia observed in these animals produces a constant demand for red blood cells (RBCs), thereby possibly leading to the recruitment of the HSC pool, wherein the $CD93^+$ subpopulation, due to their active primed phenotype, will react faster in promoting the maintenance of the circulating RBCs while keeping the dHSC population protected.

From the chromatin landscape perspective, it is interesting that H4K16ac levels decrease upon HSC aging (*14*, *15*, *62*) but can be partially restored using CASIN, a Cdc42 Rho GTPase inhibitor (*62*). In LSCs, however, reduction of H4K16ac was associated with increased stemness (*73*), arguing that altered H4K16ac levels might have different context-specific consequences. Likewise, CD93 appears to be expressed in chronic myeloid leukemia (CML) cells and promotes stemness and self-renewal of CML LSCs (*56*, *74*). Unfortunately, the H4K16ac levels of this cell type have not been defined yet. Our results support the notion that H4K16ac levels promote different outcomes depending on the cellular status, since $Mof^{+/-}$ $CD93^+$ HSCs not only show enhanced proliferation capacity but were also able to maintain their self-renewal capacity, unlike $Mof^{+/+}$ $CD93^+$ HSCs. Moreover, we observed an increase in the number of $CD93^+$ HSCs in the absence of a mature adaptive immune system. Therefore, it is tempting to speculate that decreased levels of MOF in HSCs and the expansion of the $CD93^+$ HSC population might have a proleukemic potential. This is based on our observations of their increased proliferation capacity at the expense of their self-renewal ability. In this context, this premise sheds light on the *Mof*-cancer paradox in which MOF levels are closely and positively correlated with cell proliferation (*75*), despite the fact that several cancers, including leukemia, show low MOF levels (*40*). Reduced *MOF* levels in leukemia are not sufficiently low to adversely affect cell proliferation but sufficiently low to present an impediment to HSC differentiation, which might increase the risk of malignant transformation.

MOF can be found in association with two distinct complexes, the male-specific lethal (MSL) and the nonspecific lethal (NSL/KANSL). It is known that these complexes have different histone H4 lysine residue specificities (*76*). Thereby, considering the strong anticorrelation between CD93 and H4K16ac, and lack of correlation between CD93 and either H4K5ac or H4K8ac, leads us to propose that the leukemic-like phenotype is very likely elicited by MOF in conjunction with the MSL complex. In support of this hypothesis, we had previously shown that hematopoietic system–specific knockouts of *Kansl2* or *Kansl3* do not recapitulate the same phenotype as knockout of *Mof*. Conditional *Kansl2* and *Kansl3* knockout animals developed erythroid differentiation defects but did not show the changes in the myeloid compartment nor in total HSC number observed upon deletion of *Mof* (*37*).

In terms of cellular interaction, our study showed a switch toward adaptive immune cells and $CD93^+$ HSCs in situ. By depleting mature T and B cells from $Mof^{+/-}$ animals, we found a significant increase in the $CD93^+$ HSCs accompanied by the onset of monocytic disorders. This suggests that immune surveillance might play a crucial role in controlling $CD93^+$ HSC numbers and preventing the onset of circulating immature monocytes in $Mof^{+/-}$ animals. Adaptive immune cells thereby seem to help restrain any undesirable consequence of imbalances in HSC heterogeneity.

Furthermore, CD93 was first described as a marker for early B cells and fetal HSCs, both cell types known for their proliferative

expansion capacities. Considering our findings, it will be interesting to study whether H4K16ac levels are also altered in those cell types or whether this represents an adult HSC-specific phenotype.

In addition, it is important to point out that while our study identifies $CD93^+$ as a marker for an intermediate HSC status, a detailed characterization of the $CD93^-$ HSC pool is still lacking. We envision that further studies in the $CD93^-$ HSC pool might shed light on a better deconvolution of the dHSC and aHSC transition. On the basis of our scRNA-seq data, we propose that the addition of CD27, CD47, and CD74 could be helpful to discriminate the remaining HSCs populations from the $CD93^-$ HSC pool.

In conclusion, our study shows the importance of MOF levels in governing HSC heterogeneity, since low levels of H4K16ac in vivo resulted in the accumulation of an otherwise rare HSC population that expresses CD93 on their membrane. This HSC subpopulation is akin to the G_0-G_{alert} (*46*) stem population in that it shows molecular hallmarks of both dHSCs and aHSCs, thereby likely representing a distinct intermediate cellular state that is more prone to respond upon hematopoietic stress. The fact that the CD93 marker is both extracellular and evolutionarily conserved in mammals lends itself to the isolation of live cells representing this intermediate cell population from humans. Further studies are required to explore whether the exclusion of $CD93^+$ HSCs before human bone marrow transplantation could be used to improve tissue engraftment. In addition, our findings in AML place MOF as both a potential biomarker for early detection and as a druggable target. Implementing conventional AML therapy together with an H4K16ac-selective HDAC inhibitor might help to reduce the number of highly proliferative $CD93^+$ HSC cells.

MATERIALS AND METHODS

Ethics statement

Animals were kept on a 14-hour/10-hour light-dark cycle and provided with standard chow food and water ad libitum. Every mouse strain in this study was backcrossed with C57BL/6J mice. All animal procedures are in agreement with and approved by the responsible Animal Welfare Committees (Regierungspräsidium Freiburg, Karlsruhe/Germany, license 35-9185.81/G-19/37).

Mouse strains

*Kat8*tm1Avo allele was published elsewhere (*37*, *77*), and the line *Rag-1* KO was imported from the Jackson laboratory (JAX002216). Eight- to 12-week-old mice from both sexes were randomly allocated to experimental groups. Eight-week-old male animals were used for RNA-seq and ATAC-seq.

Cell culture

Culture of the HPC7 (murine hematopoietic progenitor cell line CVCL_RB19) cell line was performed as in (*37*). Raji (CVCL_0511), SKNO1 (CVCL_2196), HL-60 (CVCL_0002), KG-1 (CVCL_0374), and U937 (CVCL_0007) were kept in Dulbecco's modified Eagle's medium (Gibco) with 10% fetal calf serum (FCS), penicillin (100 U/ml), and streptomycin (100 μg/ml). Cells were cultured in a humidified incubator at 37°C and 5% CO_2.

For the proliferation assessment, the cells were harvested every second day for 4 days, and living cells were counted by trypan blue staining. The CD93 levels were determined by FACS.

Fluorescence-activated cell sorting

Cell suspensions and flow cytometry

For flow cytometry analysis, we followed the protocol described in (*37*). Briefly, mouse bone marrow cells were isolated by flushing them with cold phosphate-buffered saline (PBS) containing 2% FCS. Next, lysis of erythrocytes was performed using the ammonium-chloride-potassium (ACK) lysing buffer (Thermo Fisher Scientific), followed by lineage-positive cell depletion using the MojoSort Mouse Hematopoietic Progenitor Cell Isolation Kit (BioLegend, #48003). Total bone marrow was incubated with a biotin antibody cocktail, and purification was performed with magnetic streptavidin nanobeads from the kit. Last, $CD93^+$ and $CD93^-$ HSCs ($LSK^+CD34^-Flt3^-CD48\text{-}CD150^+$) were sorted using a FACSAria Fusion II cytometer (BD).

Different collection approaches were applied depending on the experiment. For reverse transcription quantitative polymerase chain reaction (RT-qPCR)/immunoblot, sorted cells were collected into ice-cold PBS. For scRNA-seq, cells were sorted into 384-well plates loaded with an RNA lysis buffer [original data from (*37*)]. For single-cell clonal assessment, HSCs were sorted into 96-well plates coated with either MethoCult (STEMCELL Technologies, #M3434) or 96-well plates coated with inactive OP9 in Iscove's modified Dulbecco's medium (IMDM)–10% supplemented with stem cell factor (SCF) and thrombopoietin (TPO) cocktails. Sort purity was >90% in all cases. FACS analyses were conducted by FlowJo v.10.

Intracellular staining

For intracellular immunostaining of primary cells, we followed the protocol performed in (*37*). Briefly, progenitor cells were stained for cell surface molecules and then fixed and permeabilized using the "Perm/Fix" solution from the eBioscience Foxp3/Transcription Factor Staining Buffer Set (Affymetrix, eBioscience, USA, #00-5523-00), as described in the manufacturer's protocol. After adding the primary antibody, samples were kept at 4°C for 1 hour. The cells were then washed with wash buffer (Affymetrix, eBioscience, USA, #00-5523-00) and washed twice in FACS buffer [PBS, 0.2% bovine serum albumin (BSA), and 0.1 mM EDTA]. Last, the cells were resuspended in the FACS buffer (PBS, 0.2% BSA, and 0.1 mM EDTA) and measured using the Fortessa II/I flow cytometer (BD).

The following antibodies were used for flow cytometry: lineage-negative cocktail fluorescein isothiocyanate (FITC; 1:100; BioLegend, #13:3302; clone: 7A2,RB6-8C5,RA3-6B2,Ter119,M1/70) (1:50; FITC: CD34; BD Bioscience, #553733; clone: RAM34), c-Kit–APC (allophycocyanin) (1:300; BioLegend, #105812; clone: 2B8), Sca-1–BV421 (1:300; BioLegend, #108128; clone: D7), Ftl3-PE (phycoerythrin)–CF594 (1:600; BD Bioscience, #562537; clone: A2F10), CD34–Alexa Fluor 700 (1:50; BD Bioscience, #560518; clone:RAM34), CD48-APC-Cy7 (1:500; BioLegend, #103431; clone: HM48-1), CD150-BV510 (1:100; BioLegend, #115929; clone: TC15-12F12.2), Ter119-PE (1:300; BD Bioscience, #553673; clone: ter-119), CD11b-APC-Cy7 (1:200; BD Bioscience, #557657 and BioLegend; clone: M1/70), CD45.1-APC (1:100; BioLegend, #110713; clone: A20), CD45.2 (1:200; BioLegend, #109808; clone: 104), CD19-PE-Cy7 (1:500; BD Bioscience, #561739; clone: 1D3), CD3-APC or PerCP (peridinin chlorophyll protein)–Cy5.5 (1:500; BioLegend, #100235 and #100217; clone: 17A2), CD93-PE/APC (1:100; BioLegend, APC: 136509; PE: 136503; clone: AA4.1), C-C motif chemokine receptor 2 (CCR2) (1:200; BV41: BD Bioscience, #747963; clone: 475301), Ki67 (1:100; FITC; BD, #556026; clone: B56), A488-CDK6 (1:200; Abcam, #ab54576), MOF (1:200; Abcam, #ab200660), and H4K16ac-A488 (1:300; Millipore, #07-329).

CFSE cell staining dye

For proliferation assessment, progenitor cells were stained with 5 μM CFSE (#C34554, Invitrogen, Thermo Fisher Scientific) following the manufacturer's protocol. For proliferation analysis, we applied the preset plugin from FlowJo 10.3 (*41*).

Dihydroethidium staining for ROS detection

Freshly isolated and enriched lineage-negative cells (HSPCs) were incubated for 15 min with 5 μM dihydroethidium (Thermo Fisher Scientific, #D11347) in PBS. ROS measurements were conducted in the BD Fortessa II cytometer and analyzed in FlowJo v.10.

Total mitochondrial mass quantification

To obtain the mitochondrial mass information, the cells were stained with MitoTracker green dye (Life Technologies, #M7512), and mitochondria were labeled with 1 mM dye for 1 hour at 37°C and 5% CO_2. Cells were washed twice with PBS-BSA (0.1%), and mitochondrial mass measurements were conducted in the BD Fortessa II cytometer and analyzed in FlowJo v.10.

Preparation of OP9 feeder cell layer

OP9 feeder cells were grown in 1× IMDM (Gibco, #12561-056) supplemented with 10% FCS (Gibco, #A10491-01) and 1× penicillin/streptomycin (Gibco, #10378016). OP9 cells were grown until 80% confluence and detached using trypsin-EDTA (Gibco, 25200056) at 37°C for 5 min. Cells were resuspended in fresh complete IMDM medium, and cell concentration was adjusted to seed approximately 20,000 to 30,000 cells in 100 μl of medium per well of a 96-well plate.

CFU assay

Cell culture of sorted hematopoietic progenitors for clonal proliferation assessment

Single-cell–sorted $CFSE^+$ HSC (see "CFSE cell staining dye" section) were seeded onto mitomycin C–treated OP9 feeder cells. Cell was plated in one well of a 96-well plate and grown in 200 μl of IMDM-10% medium at 37°C and 5% CO_2. For maintenance the sorted HSCs were kept in IMDM medium (Gibco, #12440053), supplemented with 1x penicillin/streptomycin (Gibco, 10378016), 10% FCS, recombinant murine SCF (100 ng/ml; PeproTech, #250-03), and recombinant murine TPO (10 ng/ml; PeproTech, #315-14).

Bulk CFU culture and serial plating experiments

Bulk CFU culture and serial plating experiments were performed as in (*37*). In which, 100 HSCs ($LSK^+CD34^-Flt3^-CD150^+CD48^-$) $CD93^+$ or $CD93^-$ from 8- to 10-week-old mice were sorted by FACSAria Fusion II (BD). The cells were labeled or not with CFSE as indicated in the figure legends. Sorted HSCs were cultured in MethoCult (STEMCELL Technologies, #M3434) in technical duplicates. After 10 days in culture, the CFU capacity was evaluated by visual inspection. Then, we conducted serial plating with 10,000 cells originated from the primary CFU assay that were transferred to a new 24-well plate and cultured in MethoCult (STEMCELL Technologies, #03434). Next, after 10 days, colonies were quantified. In addition, downstream experiments to evaluate the daughter cells were conducted.

Chromatin accessibility with visualization technology (ATAC-see)

For ATAC-see, we followed the published protocol in (*78*). Briefly, labeled oligonucleotides (Tn5ME-A-ATTO488 or A555, Tn5ME-B-ATTO488 or A555, and Tn5MErev) were denatured at 95°C and slowly annealed to room temperature in a thermocycler. The hyperactive Tn5 (Nextera Illumina, #1502824) was assembled according to (*78*).

For immunofluorescence, we followed the protocol in (*37*), wherein colonies with high and low output were harvested and fixed with 1% methanol-free formaldehyde (Sigma-Aldrich) for 10 min at room temperature and centrifuged onto the glass slide with cytospin, 1000 rpm for 5 min, 10,000 to 30,000 cells per slide. After fixation, the cells were permeabilized with lysis buffer [10 mM tris-HCl (pH 7.4), 10 mM NaCl, 3 mM $MgCl_2$, and 0.01% IGEPAL CA-630] for 10 min. Slides were washed with PBS and blocked with blocking solution [1% BSA in PBS with 0.1% Tween 20 (PBST 0.1%)] for 1 hour at room temperature in constant movement on a shaker, followed by three PBST 0.1% washes for 10 min each. Primary antibodies diluted in PBS (1:200, MOF; Abcam, #ab200660; or 1:400, H4K16ac; Millipore, #07-32) were incubated overnight at 4°C. PBST 0.1% washes were followed by 40-min incubation with secondary antibody (1:10,000; goat anti-rabbit A594, Thermo Fisher Scientific, #A-11037). Last, the slides were incubated with transposase mixture solution (100 nM Tn5-ATTO-488N in a total volume of 50 μl of 1× Tagment DNA buffer L) at 37°C in a humidified chamber for 30 min and washed with PBST 0.1% three times for 10 min each. Coverslips were mounted using Fluoromount-G with 4′,6-diamidino-2-phenylindole (DAPI; Thermo Fisher Scientific, #F4680). Slides were imaged with Zeiss Observer Z1 with the CSU-X1 spinning disk head (Yokogawa) and the Axiocam camera (Zeiss), and images were analyzed with Fiji ImageJ software.

Tissue histology and three-dimensional reconstruction

Bone sections

Tibia was fixed with 4% paraformaldehyde (PFA) in PBS and incubated with PBS–0.5 M EDTA for 1 week at 4°C. Every second day, the solution was changed. After demineralization, tissue was embedded into optimal cutting temperature (OCT) freezing medium (Tissue-Tek, SA62550-01) and frozen gradually: First, the blocks were left on a dry ice board for 15 min, followed by liquid nitrogen submersion. OCT blocks were sectioned with a cryotome (Leica) at −20°C into 7- to 10-μm slides using the sturkey gold microtome blades (Thermo Fisher Scientific).

Whole-mount tissue

Whole tissue staining was conducted by following the bone clarity protocol (*79*). Briefly, tibia was fixed with 4% PFA in PBS overnight. After, bone was decalcified using a 10% PBS-EDTA for 14 days under constant spinning. The solution was changed every second day. The decalcified bone that was then embedded in 4% PBS-acrylamide for hydrogel stabilization to prevent protein loss is carried out (purple). The tissue is incubated in a hydrogel composed of 4% acrylamide with 0.25% VA044 in PBS at 4°C under constant stirring for 16 hours. Afterward, the hydrogel is degassed with nitrogen gas and polymerized at 37°C. Delipidation is carried out with 8% SDS in PBS (pH 7.4) at 37°C under constant stirring for 4 days, followed by a wash step with PBS and heme removal from the tissue performed with 25% amino alcohol in PBS (pH 9) at 37°C under constant stirring for 1 day. A second wash step is performed on the tissue. Last, the tissue refractive index matched (RIMS) was conducted until 1.47 RIMS.

Samples were then incubated with A488-H4K16ac (1:200) and PE-Lineage (as FACS, including CD34 and CD48; 1:100) for 4 days at 4°C under constant spinning. Afterward, samples were washed with PBST 0.1% and labeled with DAPI overnight at 4°C under constant spinning. Last, the samples were washed with PBST 0.1% twice. Bone images were acquired using Zeiss LightSheet, and reconstruction was conducted using the Imaris stitching and viewer softwares.

Western blots

As described in (*37*), for whole-cell extracts, cells were lysed in 50 mM NaCl, 1.0% IGEPAL CA-630, and 50 mM tris-HCl (pH 8.0). Buffer was supplemented with cOmplete (Roche, #4693132001) and PhosSTOP (Roche, #4906845001). Protein concentration was determined by a Qubit protein assay reagent (Thermo Fisher Scientific, #Q33212). Samples were denatured at 95°C for 5 min in a Roti-Load reducing buffer (Carl Roth, #K929.1) before SDS–polyacrylamide gel electrophoresis using NuPAGE bis-tris gels and then transferred to 0.45 μM polyvinylidene difluoride membranes. Membranes were blocked for 30 min with 5% milk in PBS with 0.3% Tween 20 (PBST 3%). Membranes were washed twice with PBST 3%. The membrane was incubated with primary antibodies against MOF (1:1000; Bethyl, #A300-992A), actin (1:10,000; Sigma-Aldrich, #A2066), H3 (1:5000; Active Motif, #39763), $p16^{INKA}$ (1:1000; Abcam, #ab54210), $p19^{INKD}$ (1:1000; Abcam, #ab80), and H4K16ac (1:2000; Millipore, #07-32) diluted in PBS–5% BSA. The membrane was then incubated with PBS–5% BSA containing horseradish peroxidase–conjugated anti-mouse (GE Healthcare, #NA931-1ML) or anti-rabbit (GE Healthcare, #NA934) (1:10,000).

RNA extraction

For RNA extraction, we followed the protocol described in (*37*). Briefly, after sorting, primary cells were pelleted at 5000*g* and lysed in TRIzol (Invitrogen, #15596026). RNA was isolated using chloroform followed by extraction and precipitation of the aqueous phase using 5 μg of ribonuclease-free glycogen and 0.25 ml of isopropanol. The supernatant was discarded, and the pellet was washed twice in 80% ethanol (EtOH) and lastly dissolved in 10 μl of H_2O. For next-generation sequencing data, the RNA was extracted using the PicoPure RNA Isolation Kit (Thermo Fisher Scientific, #KIT0204) following the manufacturer's instructions. After purification, the RNA was reversely transcribed into cDNA using the SuperScript III RT (Thermo Fisher Scientific, #18080-093). RT-qPCR reactions were performed using the SYBR Green Master Mix (Roche, #4309155); the mix contained 6.25 μl of SYBR, 0.75 μl of primers (forward and reverse; 300 nM), and 4.5 μl of H_2O.

Bulk mRNA-seq

$CD93^+$ and $CD93^-$ HSCs from 8-week-old male mice were sorted following the "Fluorescence-activated cell sorting" section. RNA was extracted using the PicoPure RNA Isolation Kit (Thermo Fisher Scientific, #KIT0204). The quality between was evaluated using the Fragment Analyzer. RNA that passed the quality control (QC) was then used to generate libraries using the NEBNext Library Low Input Library Preparation. The manufacturer's recommendations were followed, and the libraries were sequenced on an Illumina NovaSeq6000 sequencer. All sequencing data were performed in three biological replicates, having a total depth of 15 million reads per reads. The reads were conducted at 2 × 50 base pair (bp) of length.

Bulk RNA-seq bioinformatic analysis

Reads for mouse bulk RNA-seq datasets were mapped following the default snakePipes parameters of bulk RNA-seq pipeline (*80*). Briefly, STAR software alignment was used against mouse genome version GRCm38. The total number of sequenced reads averaged 15 million pairs of which mean alignment of 65% of the reads were uniquely mapped. Reads were counted with featureCounts (subread-1.5.0-p1). Differential expression analysis was performed with DESeq2 (v1.26). Multi-FASTA QC statistics–indicated data were of high quality, and sequencing depth was sufficient to test for differential expression between conditions. Differentially expressed genes were called with a FDR threshold of 0.05. Correlations between datasets and graphical output were conducted in an R environment.

Bulk ATAC-seq

$CD93^+$ and $CD93^-$ HSCs from 8-week-old male mice were sorted following the "Fluorescence-activated cell sorting" section. After sorting, cells were spinned at 1000 rpm for 5 min. Crude nuclei isolation was obtained by resuspending the pellet in 50 μl of cold lysis buffer [10 mM tris-HCl (pH 7.4), 10 mM NaCl, 3 mM $MgCl_2$, and 0.1% IGEPAL CA-630] to the samples. The samples were then centrifuged at 500*g* for 10 min at 4°C. Further processing for ATAC-seq was adapted from (*81*). Briefly, the nuclei pellet was resuspended in Tn5 reaction mix containing 2.5 μl TDE1 (Nextera Tn5 Transposase from Nextera kit; Illumina, catalog no. 15027987), 25 μl of TD (2× reaction buffer from Nextera kit), and 22.5 μl of H_2O. The tagmentation reaction took place at 37°C, shaking at 800 rpm. After precisely 30 min, the samples were placed on ice, and 250 ml of PB buffer from the MinElute PCR Purification Kit (catalog no. 28004) was added to stop the reaction. DNA purification was followed according to the manufacturer's instructions. Pure DNA was amplified using 11 PCR cycles using the NEBNext Polymerase (M0541S) for the library amplification. The ATAC-seq dataset analysis was then performed on the DNA-mapping pipeline described in snakePipes (*80*). Briefly, the adaptors were trimmed from the reads using trimGalore2 following the filtering for uniquely mapped reads and the removal of duplicates. Bowtie2 software was used for mapping using default parameters. Furthermore, the ATAC-seq pipeline from the same tool (*80*) was applied for open chromatin peak calling using MACS2 tools.

scRNA-seq analysis

Single-cell sorting and RNA and library preparation from single cells were previously described elsewhere (*37*). Briefly, the following gating strategy was used to sort the populations present in the scRNA-seq analysis: megakaryocyte progenitor ($Lin^-Sca\text{-}1^-c\text{-}Kit^+CD150^+CD41^+$, 48 cells were sorted), GMP ($Lin^-Sca\text{-}1^-c\text{-}Kit^+CD41^-FcγRII/III^+$, 24 cells were sorted), pre-GMP ($Lin^-Sca\text{-}1^-c\text{-}Kit^+CD41^-FcγRII/III^-CD150^-CD105^-$, 24 cells were sorted), pre-MEP ($Lin^-Sca\text{-}1^-c\text{-}Kit^+CD41^-FcγRII/III^-CD150^+CD105^-$, 48 cells were sorted), pre–CFU-E ($Lin^-Sca\text{-}1^-c\text{-}Kit^+CD41^-FcγRII/III^-CD150^+CD105^+$, 48 cells were sorted), MEP ($Lin^-Sca\text{-}1^-c\text{-}Kit^+CD150^+CD41^-FcγRII/III^-CD105^-$, 48 cells were sorted), pro erythroid ($CD71^+Ter119^{low}$, 48 cells were sorted), myeloid progenitor ($c\text{-}Kit^{high}Sca\text{-}1^-$, 768 cells were sorted), early progenitor ($LSK^+Flt3^-CD34^-$, 576 cells were sorted), LT-HSC ($LSK^+CD150^+CD48^-$, 792 cells were sorted), LSK^{high} (864 cells were sorted), and LSK^{low} (576 cells were sorted). Only cells negative for Zombie Dye (BioLegend, #423212) were included to ensure the sort of living cells.

Cells were sorted into 384-well plates loaded with RNA lysis buffer, and CEL-Seq2 (*82*) single-cell library preparation that was conducted using a nanoliter pipetting robot (mosquito HTS, TTP Labtech) was used to reduce the CEL-Seq2 protocol's original volumes by fivefold.

Single-cell data analysis

For transcript quantification, we followed the analysis described in (*37*, *43*). Briefly, paired-end reads were aligned to the transcriptome

using the bwa software (version 0.6.2-r126), with default parameters. The transcriptome contained all gene models based on the mouse ENCODE VM9 release downloaded from the University of California, Santa Cruz genome browser comprising 57,207 isoforms derived from 57,207 gene loci with 57,114 isoforms mapping to fully annotated chromosomes (1 to 19, X, Y, and mitochondrial). All isoforms for the same gene were merged to a single gene locus, and gene loci were merged if loci overlapped by >75%. This procedure resulted in 34,111 gene groups. The right mate of each read pair was mapped to all gene groups and to the set of 92 ERCC spike-ins in sense direction. Multimapper reads were discarded. The left mate contains the barcode information: In the dataset, the first six bases represent the cell-specific barcode, and the following six bases correspond to the Unique Molecular Identifier (UMI). The residue of the left read contains the polyT stretch and the adjacent gene sequence. For each cell barcode and gene locus, the number of UMIs was aggregated and, on the basis of binomial statistics (*37*, *43*), converted into transcript counts.

Cell identification using Seurat

Seurat version 4 (*83*, *84*) was used for cell cluster assignment of all sorted cell types. We started by loading the CEL-Seq transcript counts as a Seurat object. Followed by QC metrics and filtering in which low-quality cells or empty droplets were removed by filtering the cells that have unique feature counts of more than 500 or less than 5 features, we also removed the cells having >5% mitochondrial counts. The remaining data were then normalized by a global scaling normalization method, namely, "LogNormalize," followed by the identification of highly variable features. The resulting list was used to evaluate the dataset variability by principal components analysis (PCA) plots.

Next, we applied a linear transformation ("scaling") and evaluated the dataset dimensionality by comparing the distribution of *P* values for each PC with a uniform distribution using the JackStraw Plot and further validated by the "elbow plot." The cell clusters were then determined by constructing a *k*-nearest neighbors (knn) graph based on the Euclidean distance in PCA space using 1:15 as dimensionality parameters. Next, to cluster the cells, we applied the Louvain algorithm to iteratively group cells together; with the goal of optimizing the standard modularity function, we set a 0.5 resolution. The data were then visualized using the nonlinear dimensionality reduction uniform manifold approximation and projection (UMAP).

HSCs rare cell type identification

Subpopulation bioinformatics analysis from HSCs was conducted in the R environment. For identification of rare and abundant cell types, we applied the RaceID3 algorithm (*43*) and the parameters described in (*37*).

Inference of lineage trees using StemID3

StemID was used to infer lineage trees and HSC continuum activation based on pseudotemporal ordering of single-cell transcriptomes (*43*, *85*). To this end, RaceID3 cluster prediction was used. To assign cells to intercluster links, we applied the strategy, considering the projection of a vector connecting a cluster medoid to a member cell of the same cluster onto the links from the medoid of its cluster to the medoids of all other clusters. The longest projection identifies the link that this cell is assigned to and defines the projection coordinate. As parameters, we only consider clusters with >5 cells and 1000 randomizations of cell positions used to compute projection of cell on intercluster links. The score threshold for links was defined as 0.2. Statistical significance was determined as 0.01.

Expression variability and transition state probability using VarID

VarID (*44*) was used to identify locally homogeneous neighborhoods in cell state space. To this end, we first determined the baseline variability using the pruneKnn() function, in which the number of knn was setted as 10, and Euclidean distance matrix used as a distance matrix. Next, we determined the transition probabilities in a dimensional reduction representation of the RaceID SCseq object. The local gene expression variability across the pruned knn at a given link probability was determined by the compNoise() function. In addition, the genes with significantly elevated variability in a cluster was calculated with the diffNoistGenes() function; this function uses the Wilcoxon rank sum test between cells in a cluster and all remaining cells. Statistical significance was determined as 0.01. VarID documentation can be found at https://cran.r-project.org/web/packages/RaceID/vignettes/RaceID.html.

Ligand-receptor interaction

The cross-talk between $CD93^+$ HSCs and immune cells were predicted using a computational approach by applying the identifying and illustrating alterations in intracellular signaling network (iTalk) software (*86*). After cellular identifications, the metadata sheet containing the sample name and cellular identity and a normalized count sheet (from Seurat) were loaded in the R environment. Then, iTalk was initiated to capture highly abundant ligand-receptor transcript pairs. We set the rawParse() parameters as top_genes = 50 and stat = 'median.'

Pseudotime ordering of dHSC and aHSCs

Published available scRNA-seq from sorted dHSC and aHSCs (*45*) was submitted into the STREAM (*87*) pipeline. Random sorted dHSC was used as a root cell. For pseudotime analysis, we followed the original pipeline and plotted the diffusion map using the Python environment.

BrDU incorporation in vivo

IFN-α challenged

For the IFN-α treatment, 8- to 12-week-old mice were subcutaneously injected with mouse recombinant IFN-α (10^4 U) diluted in PBS four times at 2-day interval rate as performed in (*88*).

BrdU pulsing

After 7 days, treated animals received two intraperitoneal injections of BrdU (1 mg/100 μl of PBS), with an interval of 6 hours between the injections. Two hours after second injection, animals were euthanized as in (*89*). Bone marrow cells were isolated as described in the "Fluorescence-activated cell sorting" section. HSCs proliferation was evaluated by flow cytometry based on BrdU incorporation (1:100; BV510, BD, #563445; clone: 3D4).

Quantification and statistical analysis

Data are presented as means ± SEM or SD indicated in the figure legend. Each experiment was performed with a minimum of three biological replicates; exact numbers are mentioned in associated figure legends. Except scRNA-seq analysis, all statistical analyses were performed using Prism 6 software (GraphPad). The statistical tests used and relevant *P* values are mentioned in appropriate figures/figure legends. *P* values of <0.05 were considered significant.

SUPPLEMENTARY MATERIALS

Supplementary material for this article is available at http://advances.sciencemag.org/cgi/content/full/7/32/eabi5987/DC1

View/request a protocol for this paper from *Bio-protocol*.

REFERENCES AND NOTES

1. S. H. Orkin, L. I. Zon, Hematopoiesis: An evolving paradigm for stem cell biology. *Cell* **132**, 631–644 (2008).
2. B. Dykstra, D. Kent, M. Bowie, L. McCaffrey, M. Hamilton, K. Lyons, S.-J. Lee, R. Brinkman, C. Eaves, Long-term propagation of distinct hematopoietic differentiation programs in vivo. *Cell Stem Cell* **1**, 218–229 (2007).
3. C. E. Muller-Sieburg, H. B. Sieburg, J. M. Bernitz, G. Cattarossi, Stem cell heterogeneity: Implications for aging and regenerative medicine. *Blood* **119**, 3900–3907 (2012).
4. C. E. Muller-Sieburg, H. B. Sieburg, Clonal diversity of the stem cell compartment. *Curr. Opin. Hematol.* **13**, 243–248 (2006).
5. E. Verovskaya, M. J. C. Broekhuis, E. Zwart, M. Ritsema, R. van Os, G. de Haan, L. V. Bystrykh, Heterogeneity of young and aged murine hematopoietic stem cells revealed by quantitative clonal analysis using cellular barcoding. *Blood* **122**, 523–532 (2013).
6. A. Wilson, E. Laurenti, G. Oser, R. C. van der Wath, W. Blanco-Bose, M. Jaworski, S. Offner, C. F. Dunant, L. Eshkind, E. Bockamp, P. Lió, H. R. Macdonald, A. Trumpp, Hematopoietic stem cells reversibly switch from dormancy to self-renewal during homeostasis and repair. *Cell* **135**, 1118–1129 (2008).
7. H. Ema, Y. Morita, T. Suda, Heterogeneity and hierarchy of hematopoietic stem cells. *Exp. Hematol.* **42**, 74–82.e2 (2014).
8. A. E. Rodriguez-Fraticelli, C. Weinreb, S.-W. Wang, R. P. Migueles, M. Jankovic, M. Usart, A. M. Klein, S. Lowell, F. D. Camargo, Single-cell lineage tracing unveils a role for TCF15 in haematopoiesis. *Nature* **583**, 585–589 (2020).
9. C. Weinreb, A. Rodriguez-Fraticelli, F. D. Camargo, A. M. Klein, Lineage tracing on transcriptional landscapes links state to fate during differentiation. *Science* **367**, (2020).
10. S. Haas, A. Trumpp, M. D. Milsom, Causes and consequences of hematopoietic stem cell heterogeneity. *Cell Stem Cell* **22**, 627–638 (2018).
11. G. A. Challen, D. Sun, A. Mayle, M. Jeong, M. Luo, B. Rodriguez, C. Mallaney, H. Celik, L. Yang, Z. Xia, S. Cullen, J. Berg, Y. Zheng, G. J. Darlington, W. Li, M. A. Goodell, Dnmt3a and Dnmt3b have overlapping and distinct functions in hematopoietic stem cells. *Cell Stem Cell* **15**, 350–364 (2014).
12. F. Pastore, R. L. Levine, Epigenetic regulators and their impact on therapy in acute myeloid leukemia. *Haematologica* **101**, 269–278 (2016).
13. C. P. Rodrigues, M. Shvedunova, A. Akhtar, Epigenetic regulators as the gatekeepers of hematopoiesis. *Trends Genet.* **37**, 125–142 (2021).
14. M. C. Florian, M. Klose, M. Sacma, J. Jablanovic, L. Knudson, K. J. Nattamai, G. Marka, A. Vollmer, K. Soller, V. Sakk, N. Cabezas-Wallscheid, Y. Zheng, M. A. Mulaw, I. Glauche, H. Geiger, Aging alters the epigenetic asymmetry of HSC division. *PLOS Biol.* **16**, e2003389 (2018).
15. A. Grigoryan, N. Guidi, K. Senger, T. Liehr, K. Soller, G. Marka, A. Vollmer, Y. Markaki, H. Leonhardt, C. Buske, D. B. Lipka, C. Plass, Y. Zheng, M. A. Mulaw, H. Geiger, M. C. Florian, LaminA/C regulates epigenetic and chromatin architecture changes upon aging of hematopoietic stem cells. *Genome Biol.* **19**, 189 (2018).
16. M. Saçma, J. Pospiech, R. Bogeska, W. de Back, J.-P. Mallm, V. Sakk, K. Soller, G. Marka, A. Vollmer, R. Karns, N. Cabezas-Wallscheid, A. Trumpp, S. Méndez-Ferrer, M. D. Milsom, M. A. Mulaw, H. Geiger, M. C. Florian, Haematopoietic stem cells in perisinusoidal niches are protected from ageing. *Nat. Cell Biol.* **21**, 1309–1320 (2019).
17. P. Rimmelé, C. L. Bigarella, R. Liang, B. Izac, R. Dieguez-Gonzalez, G. Barbet, M. Donovan, C. Brugnara, J. M. Blander, D. A. Sinclair, S. Ghaffari, Aging-like phenotype and defective lineage specification in SIRT1-deleted hematopoietic stem and progenitor cells. *Stem Cell Reports* **3**, 44–59 (2014).
18. H. Oguro, J. Yuan, H. Ichikawa, T. Ikawa, S. Yamazaki, H. Kawamoto, H. Nakauchi, A. Iwama, Poised lineage specification in multipotential hematopoietic stem and progenitor cells by the polycomb protein Bmi1. *Cell Stem Cell* **6**, 279–286 (2010).
19. H. Oguro, A. Iwama, Y. Morita, T. Kamijo, M. van Lohuizen, H. Nakauchi, Differential impact of *Ink4a* and *Arf* on hematopoietic stem cells and their bone marrow microenvironment in *Bmi1*-deficient mice. *J. Exp. Med.* **203**, 2247–2253 (2006).
20. H. Xie, J. Xu, J. H. Hsu, M. Nguyen, Y. Fujiwara, C. Peng, S. H. Orkin, Polycomb repressive complex 2 regulates normal hematopoietic stem cell function in a developmental-stage-specific manner. *Cell Stem Cell* **14**, 68–80 (2014).
21. I. Hidalgo, A. Herrera-Merchan, J. M. Ligos, L. Carramolino, J. Nuñez, F. Martinez, O. Dominguez, M. Torres, S. Gonzalez, Ezh1 is required for hematopoietic stem cell maintenance and prevents senescence-like cell cycle arrest. *Cell Stem Cell* **11**, 649–662 (2012).
22. M. Jones, J. Chase, M. Brinkmeier, J. Xu, D. N. Weinberg, J. Schira, A. Friedman, S. Malek, J. Grembecka, T. Cierpicki, Y. Dou, S. A. Camper, I. Maillard, *Ash1l* controls quiescence and self-renewal potential in hematopoietic stem cells. *J. Clin. Invest.* **125**, 2007–2020 (2015).
23. I. Maillard, Y.-X. Chen, A. Friedman, Y. Yang, A. T. Tubbs, O. Shestova, W. S. Pear, X. Hua, Menin regulates the function of hematopoietic stem cells and lymphoid progenitors. *Blood* **113**, 1661–1669 (2009).
24. B. E. Li, T. Gan, M. Meyerson, T. H. Rabbitts, P. Ernst, Distinct pathways regulated by menin and by MLL1 in hematopoietic stem cells and developing B cells. *Blood* **122**, 2039–2046 (2013).
25. M. Heuser, D. B. Yap, M. Leung, T. R. de Algara, A. Tafech, S. McKinney, J. Dixon, R. Thresher, B. Colledge, M. Carlton, R. K. Humphries, S. A. Aparicio, Loss of MLL5 results in pleiotropic hematopoietic defects, reduced neutrophil immune function, and extreme sensitivity to DNA demethylation. *Blood* **113**, 1432–1443 (2009).
26. E. L. Artinger, B. P. Mishra, K. M. Zaffuto, B. E. Li, E. K. Y. Chung, A. W. Moore, Y. Chen, C. Cheng, P. Ernst, An MLL-dependent network sustains hematopoiesis. *Proc. Natl. Acad. Sci. U.S.A.* **110**, 12000–12005 (2013).
27. A.-M. Bröske, L. Vockentanz, S. Kharazi, M. R. Huska, E. Mancini, M. Scheller, C. Kuhl, A. Enns, M. Prinz, R. Jaenisch, C. Nerlov, A. Leutz, M. A. Andrade-Navarro, S. E. W. Jacobsen, F. Rosenbauer, DNA methylation protects hematopoietic stem cell multipotency from myeloerythroid restriction. *Nat. Genet.* **41**, 1207–1215 (2009).
28. J. J. Trowbridge, J. W. Snow, J. Kim, S. H. Orkin, DNA methyltransferase 1 is essential for and uniquely regulates hematopoietic stem and progenitor cells. *Cell Stem Cell* **5**, 442–449 (2009).
29. G. A. Challen, D. Sun, M. Jeong, M. Luo, J. Jelinek, J. S. Berg, C. Bock, A. Vasanthakumar, H. Gu, Y. Xi, S. Liang, Y. Lu, G. J. Darlington, A. Meissner, J.-P. J. Issa, L. A. Godley, W. Li, M. A. Goodell, Dnmt3a is essential for hematopoietic stem cell differentiation. *Nat. Genet.* **44**, 23–31 (2011).
30. F. Izzo, S. C. Lee, A. Poran, R. Chaligne, F. Gaiti, B. Gross, R. R. Murali, S. D. Deochand, C. Ang, P. W. Jones, A. S. Nam, K.-T. Kim, S. Kothen-Hill, R. C. Schulman, M. Ki, P. Lhoumaud, J. A. Skok, A. D. Viny, R. L. Levine, E. Kenigsberg, O. Abdel-Wahab, D. A. Landau, DNA methylation disruption reshapes the hematopoietic differentiation landscape. *Nat. Genet.* **52**, 378–387 (2020).
31. M. Farlik, F. Halbritter, F. Müller, F. A. Choudry, P. Ebert, J. Klughammer, S. Farrow, A. Santoro, V. Ciaurro, A. Mathur, R. Uppal, H. G. Stunnenberg, W. H. Ouwehand, E. Laurenti, T. Lengauer, M. Frontini, C. Bock, DNA methylation dynamics of human hematopoietic stem cell differentiation. *Cell Stem Cell* **19**, 808–822 (2016).
32. D. Lara-Astiaso, A. Weiner, E. Lorenzo-Vivas, I. Zaretsky, D. A. Jaitin, E. David, H. Keren-Shaul, A. Mildner, D. Winter, S. Jung, N. Friedman, I. Amit, Chromatin state dynamics during blood formation. *Science* **345**, 943–949 (2014).
33. N. Cabezas-Wallscheid, D. Klimmeck, J. Hansson, D. B. Lipka, A. Reyes, Q. Wang, D. Weichenhan, A. Lier, L. von Paleske, S. Renders, P. Wünsche, P. Zeisberger, D. Brocks, L. Gu, C. Herrmann, S. Haas, M. A. G. Essers, B. Brors, R. Eils, W. Huber, M. D. Milsom, C. Plass, J. Krijgsveld, A. Trumpp, Identification of regulatory networks in HSCs and their immediate progeny via integrated proteome, transcriptome, and DNA methylome analysis. *Cell Stem Cell* **15**, 507–522 (2014).
34. V. W. C. Yu, R. Z. Yusuf, T. Oki, J. Wu, B. Saez, X. Wang, C. Cook, N. Baryawno, M. J. Ziller, E. Lee, H. Gu, A. Meissner, C. P. Lin, P. V. Kharchenko, D. T. Scadden, Epigenetic memory underlies cell-autonomous heterogeneous behavior of hematopoietic stem cells. *Cell* **167**, 1310–1322.e17 (2016).
35. B. de Laval, J. Maurizio, P. K. Kandalla, G. Brisou, L. Simonnet, C. Huber, G. Gimenez, O. Matcovitch-Natan, S. Reinhardt, E. David, A. Mildner, A. Leutz, B. Nadel, C. Bordi, I. Amit, S. Sarrazin, M. H. Sieweke, C/EBPβ-dependent epigenetic memory induces trained immunity in hematopoietic stem cells. *Cell Stem Cell* **26**, 793 (2020).
36. T. Conrad, F. M. G. Cavalli, J. M. Vaquerizas, N. M. Luscombe, A. Akhtar, *Drosophila* dosage compensation involves enhanced Pol II recruitment to male X-linked promoters. *Science* **337**, 742–746 (2012).
37. C. P. Rodrigues, J. S. Herman, B. Herquel, C. I. K. Valsecchi, T. Stehle, D. Grün, A. Akhtar, Temporal expression of MOF acetyltransferase primes transcription factor networks for erythroid fate. *Sci. Adv.* **6**, eaaz4815 (2020).
38. M. Samata, A. Alexiadis, G. Richard, P. Georgiev, J. Nuebler, T. Kulkarni, G. Renschler, M. F. Basilicata, F. L. Zenk, M. Shvedunova, G. Semplicio, L. Mirny, N. Iovino, A. Akhtar, Intergenerationally maintained histone H4 lysine 16 acetylation is instructive for future gene activation. *Cell* **182**, 127–144.e23 (2020).
39. D. G. Valerio, H. Xu, M. E. Eisold, C. M. Woolthuis, T. K. Pandita, S. A. Armstrong, Histone acetyltransferase activity of MOF is required for adult but not early fetal hematopoiesis in mice. *Blood* **129**, 48–59 (2017).
40. W.-B. Zhao, M. Wang, S. Gao, A. S. Shaikh, J. Chen, X.-Z. Li, The histone acetyltranseferase KAT8 regulates cell differentiation by suppression of MN1 in AML. *Br. J. Haematol.* **182**, 276–279 (2018).
41. M. Roederer, Interpretation of cellular proliferation data: Avoid the panglossian. *Cytometry A* **79A**, 95–101 (2011).
42. C. E. M. Allsopp, J. Langhorne, Assessing antigen-specific proliferation and cytokine responses using flow cytometry. *Methods Mol. Med.* **72**, 409–421 (2002).
43. J. S. Herman, Sagar, D. Grün, FateID infers cell fate bias in multipotent progenitors from single-cell RNA-seq data. *Nat. Methods* **15**, 379–386 (2018).
44. D. Grün, Revealing dynamics of gene expression variability in cell state space. *Nat. Methods* **17**, 45–49 (2020).

45. N. Cabezas-Wallscheid, F. Buettner, P. Sommerkamp, D. Klimmeck, L. Ladel, F. B. Thalheimer, D. Pastor-Flores, L. P. Roma, S. Renders, P. Zeisberger, A. Przybylla, K. Schönberger, R. Scognamiglio, S. Altamura, C. M. Florian, M. Fawaz, D. Vonficht, M. Tesio, P. Collier, D. Pavlinic, H. Geiger, T. Schroeder, V. Benes, T. P. Dick, M. A. Rieger, O. Stegle, A. Trumpp, Vitamin A-retinoic acid signaling regulates hematopoietic stem cell dormancy. *Cell* **169**, 807–823.e19 (2017).
46. J. T. Rodgers, K. Y. King, J. O. Brett, M. J. Cromie, G. W. Charville, K. K. Maguire, C. Brunson, N. Mastey, L. Liu, C.-R. Tsai, M. A. Goodell, T. A. Rando, mTORC1 controls the adaptive transition of quiescent stem cells from G_0 to G_{Alert}. *Nature* **510**, 393–396 (2014).
47. M. Crisan, E. Dzierzak, The many faces of hematopoietic stem cell heterogeneity. *Development* **143**, 4571–4581 (2016).
48. C. T. J. van Velthoven, T. A. Rando, Stem cell quiescence: Dynamism, restraint, and cellular idling. *Cell Stem Cell* **24**, 213–225 (2019).
49. E. M. Pietras, D. Reynaud, Y.-A. Kang, D. Carlin, F. J. Calero-Nieto, A. D. Leavitt, J. M. Stuart, B. Göttgens, E. Passegué, Functionally distinct subsets of lineage-biased multipotent progenitors control blood production in normal and regenerative conditions. *Cell Stem Cell* **17**, 35–46 (2015).
50. A. Giladi, F. Paul, Y. Herzog, Y. Lubling, A. Weiner, I. Yofe, D. Jaitin, N. Cabezas-Wallscheid, R. Dress, F. Ginhoux, A. Trumpp, A. Tanay, I. Amit, Single-cell characterization of haematopoietic progenitors and their trajectories in homeostasis and perturbed haematopoiesis. *Nat. Cell Biol.* **20**, 836–846 (2018).
51. T. Fukushima, Y. Tanaka, F. K. Hamey, C.-H. Chang, T. Oki, S. Asada, Y. Hayashi, T. Fujino, T. Yonezawa, R. Takeda, K. C. Kawabata, T. Fukuyama, T. Umemoto, K. Takubo, H. Takizawa, S. Goyama, Y. Ishihama, H. Honda, B. Göttgens, T. Kitamura, Discrimination of Dormant and Active Hematopoietic Stem Cells by G0 Marker Reveals Dormancy Regulation by Cytoplasmic Calcium. *Cell Reports.* **29**, 4144–4158.e7 (2019).
52. T. Org, D. Duan, R. Ferrari, A. Montel-Hagen, B. Van Handel, M. A. Kerényi, R. Sasidharan, L. Rubbi, Y. Fujiwara, M. Pellegrini, S. H. Orkin, S. K. Kurdistani, H. K. Mikkola, Scl binds to primed enhancers in mesoderm to regulate hematopoietic and cardiac fate divergence. *EMBO J.* **34**, 759–777 (2015).
53. M. C. Greenlee, S. A. Sullivan, S. S. Bohlson, Detection and characterization of soluble CD93 released during inflammation. *Inflamm. Res.* **58**, 909–919 (2009).
54. E. P. McGreal, N. Ikewaki, H. Akatsu, B. P. Morgan, P. Gasque, Human C1qRp is identical with CD93 and the mNI-11 antigen but does not bind C1q. *J. Immunol.* **168**, 5222–5232 (2002).
55. E. McGreal, P. Gasque, Structure-function studies of the receptors for complement C1q. *Biochem. Soc. Trans.* **30**, 1010–1014 (2002).
56. C. Riether, R. Radpour, N. M. Kallen, D. T. Bürgin, C. Bachmann, C. M. Schürch, U. Lüthi, M. Arambasic, S. Hoppe, C. E. Albers, G. M. Baerlocher, A. F. Ochsenbein, Metoclopramide treatment blocks CD93-signaling-mediated self-renewal of chronic myeloid leukemia stem cells. *Cell Rep.* **34**, 108663 (2021).
57. R. Lugano, K. Vemuri, D. Yu, M. Bergqvist, A. Smits, M. Essand, S. Johansson, E. Dejana, A. Dimberg, CD93 promotes β_1 integrin activation and fibronectin fibrillogenesis during tumor angiogenesis. *J. Clin. Invest.* **128**, 3280–3297 (2018).
58. B. M. M. Sagar, S. Rentala, P. N. V. Gopal, S. Sharma, A. Mukhopadhyay, Fibronectin and laminin enhance engraftibility of cultured hematopoietic stem cells. *Biochem. Biophys. Res. Commun.* **350**, 1000–1005 (2006).
59. S. Ramamoorthy, K. Kometani, J. S. Herman, M. Bayer, S. Boller, J. Edwards-Hicks, H. Ramachandran, R. Li, R. Klein-Geltink, E. L. Pearce, D. Grün, R. Grosschedl, EBF1 and Pax5 safeguard leukemic transformation by limiting IL-7 signaling, Myc expression, and folate metabolism. *Genes Dev.* **34**, 1503–1519 (2020).
60. M. A. G. Essers, S. Offner, W. E. Blanco-Bose, Z. Waibler, U. Kalinke, M. A. Duchosal, A. Trumpp, IFNα activates dormant haematopoietic stem cells *in vivo*. *Nature* **458**, 904–908 (2009).
61. Z. Li, M. Philip, P. B. Ferrell, Alterations of T-cell-mediated immunity in acute myeloid leukemia. *Oncogene* **39**, 3611–3619 (2020).
62. M. C. Florian, K. Dörr, A. Niebel, D. Daria, H. Schrezenmeier, M. Rojewski, M.-D. Filippi, A. Hasenberg, M. Gunzer, K. Scharffetter-Kochanek, Y. Zheng, H. Geiger, Cdc42 activity regulates hematopoietic stem cell aging and rejuvenation. *Cell Stem Cell* **10**, 520–530 (2012).
63. M. R. Corces, J. D. Buenrostro, B. Wu, P. G. Greenside, S. M. Chan, J. L. Koenig, M. P. Snyder, J. K. Pritchard, A. Kundaje, W. J. Greenleaf, R. Majeti, H. Y. Chang, Lineage-specific and single-cell chromatin accessibility charts human hematopoiesis and leukemia evolution. *Nat. Genet.* **48**, 1193–1203 (2016).
64. V.-P. Lavallée, I. Baccelli, J. Krosl, B. Wilhelm, F. Barabé, P. Gendron, G. Boucher, S. Lemieux, A. Marinier, S. Meloche, J. Hébert, G. Sauvageau, The transcriptomic landscape and directed chemical interrogation of *MLL*-rearranged acute myeloid leukemias. *Nat. Genet.* **47**, 1030–1037 (2015).
65. X. Zhao, S. Gao, Z. Wu, S. Kajigaya, X. Feng, Q. Liu, D. M. Townsley, J. Cooper, J. Chen, K. Keyvanfar, M. D. P. Fernandez Ibanez, X. Wang, N. S. Young, Single-cell RNA-seq reveals a distinct transcriptome signature of aneuploid hematopoietic cells. *Blood* **130**, 2762–2773 (2017).
66. T. Haferlach, A. Kohlmann, L. Wieczorek, G. Basso, G. T. Kronnie, M.-C. Béné, J. De Vos, J. M. Hernández, W.-K. Hofmann, K. I. Mills, A. Gilkes, S. Chiaretti, S. A. Shurtleff, T. J. Kipps, L. Z. Rassenti, A. E. Yeoh, P. R. Papenhausen, W.-M. Liu, P. M. Williams, R. Foà, Clinical utility of microarray-based gene expression profiling in the diagnosis and subclassification of leukemia: Report from the international microarray innovations in leukemia study group. *J. Clin. Oncol.* **28**, 2529–2537 (2010).
67. A. Kohlmann, T. J. Kipps, L. Z. Rassenti, J. R. Downing, S. A. Shurtleff, K. I. Mills, A. F. Gilkes, W.-K. Hofmann, G. Basso, M. C. Dell'Orto, R. Foà, S. Chiaretti, J. De Vos, S. Rauhut, P. R. Papenhausen, J. M. Hernández, E. Lumbreras, A. E. Yeoh, E. S. Koay, R. Li, W.-m. Liu, P. M. Williams, L. Wieczorek, T. Haferlach, An international standardization programme towards the application of gene expression profiling in routine leukaemia diagnostics: The Microarray Innovations in LEukemia study prephase. *Br. J. Haematol.* **142**, 802–807 (2008).
68. P. Harris, P. Ralph, Human leukemic models of myelomonocytic development: A review of the HL-60 and U937 cell lines. *J. Leukoc. Biol.* **37**, 407–422 (1985).
69. N. Hajji, K. Wallenborg, P. Vlachos, J. Füllgrabe, O. Hermanson, B. Joseph, Opposing effects of hMOF and SIRT1 on H4K16 acetylation and the sensitivity to the topoisomerase II inhibitor etoposide. *Oncogene* **29**, 2192–2204 (2010).
70. M.-D. Filippi, S. Ghaffari, Mitochondria in the maintenance of hematopoietic stem cells: New perspectives and opportunities. *Blood* **133**, 1943–1952 (2019).
71. R. L. Bowman, L. Busque, R. L. Levine, Clonal hematopoiesis and evolution to hematopoietic malignancies. *Cell Stem Cell* **22**, 157–170 (2018).
72. S. Wingert, F. B. Thalheimer, N. Haetscher, M. Rehage, DNA-damage response gene GADD45A induces differentiation in hematopoietic stem cells without inhibiting cell cycle or survival. *Stem Cells* **34**, 699–710 (2016).
73. K. B. Kaufmann, L. Garcia-Prat, Q. Liu, S. W. K. Ng, S.-I. Takayanagi, A. Mitchell, E. Wienholds, P. van Galen, C. A. Cumbaa, M. J. Tsay, C. Pastrello, E. Wagenblast, G. Krivdova, M. D. Minden, E. R. Lechman, S. Zandi, I. Jurisica, J. C. Y. Wang, S. Z. Xie, J. E. Dick, A stemness screen reveals *C3orf54/INKA1* as a promoter of human leukemia stem cell latency. *Blood* **133**, 2198–2211 (2019).
74. R. Kinstrie, G. A. Horne, H. Morrison, D. Irvine, C. Munje, E. G. Castañeda, H. A. Moka, K. Dunn, J. E. Cassels, N. Parry, C. J. Clarke, M. T. Scott, R. E. Clark, T. L. Holyoake, H. Wheadon, M. Copland, CD93 is expressed on chronic myeloid leukemia stem cells and identifies a quiescent population which persists after tyrosine kinase inhibitor therapy. *Leukemia* **34**, 1613–1625 (2020).
75. X. Li, L. Li, R. Pandey, J. S. Byun, K. Gardner, Z. Qin, Y. Dou, The histone acetyltransferase MOF is a key regulator of the embryonic stem cell core transcriptional network. *Cell Stem Cell* **11**, 163–178 (2012).
76. Y. Cai, J. Jin, S. K. Swanson, M. D. Cole, S. H. Choi, L. Florens, M. P. Washburn, J. W. Conaway, R. C. Conaway, Subunit composition and substrate specificity of a MOF-containing histone acetyltransferase distinct from the male-specific lethal (MSL) complex. *J. Biol. Chem.* **285**, 4268–4272 (2010).
77. T. Thomas, M. P. Dixon, A. J. Kueh, A. K. Voss, Mof (MYST1 or KAT8) is essential for progression of embryonic development past the blastocyst stage and required for normal chromatin architecture. *Mol. Cell. Biol.* **28**, 5093–5105 (2008).
78. X. Chen, Y. Shen, W. Draper, J. D. Buenrostro, U. Litzenburger, S. W. Cho, A. T. Satpathy, A. C. Carter, R. P. Ghosh, A. East-Seletsky, J. A. Doudna, W. J. Greenleaf, J. T. Liphardt, H. Y. Chang, ATAC-see reveals the accessible genome by transposase-mediated imaging and sequencing. *Nat. Methods* **13**, 1013–1020 (2016).
79. A. Greenbaum, K. Y. Chan, T. Dobreva, D. Brown, D. H. Balani, R. Boyce, H. M. Kronenberg, H. J. McBride, V. Gradinaru, Bone CLARITY: Clearing, imaging, and computational analysis of osteoprogenitors within intact bone marrow. *Sci. Transl. Med.* **9**, eaah6518 (2017).
80. V. Bhardwaj, S. Heyne, K. Sikora, L. Rabbani, M. Rauer, F. Kilpert, A. S. Richter, D. P. Ryan, T. Manke, snakePipes: Facilitating flexible, scalable and integrative epigenomic analysis. *Bioinformatics* **35**, 4757–4759 (2019).
81. J. D. Buenrostro, B. Wu, H. Y. Chang, W. J. Greenleaf, ATAC-seq: A method for assaying chromatin accessibility genome-wide. *Curr. Protoc. Mol. Biol.* **109**, 21.29.1–21.29.9 (2015).
82. T. Hashimshony, N. Senderovich, G. Avital, A. Klochendler, Y. de Leeuw, L. Anavy, D. Gennert, S. Li, K. J. Livak, O. Rozenblatt-Rosen, Y. Dor, A. Regev, I. Yanai, CEL-Seq2: Sensitive highly-multiplexed single-cell RNA-Seq. *Genome Biol.* **17**, 77 (2016).
83. Y. Hao, S. Hao, E. Andersen-Nissen, W. M. Mauck III, S. Zheng, A. Butler, M. J. Lee, A. J. Wilk, C. Darby, M. Zagar, P. Hoffman, M. Stoeckius, E. Papalexi, E. P. Mimitou, J. Jain, A. Srivastava, T. Stuart, L. B. Fleming, B. Yeung, A. J. Rogers, J. M. McElrath, C. A. Blish, R. Gottardo, P. Smibert, R. Satija, Integrated analysis of multimodal single-cell data. *bioRxiv* 2020.10.12.335331 , (2020).
84. T. Stuart, A. Butler, P. Hoffman, C. Hafemeister, E. Papalexi, W. M. Mauck III, Y. Hao, M. Stoeckius, P. Smibert, R. Satija, Comprehensive integration of single-cell data. *Cell* **177**, 1888–1902.e21 (2019).
85. D. Grün, M. J. Muraro, J.-C. Boisset, K. Wiebrands, A. Lyubimova, G. Dharmadhikari, M. van den Born, J. van Es, E. Jansen, H. Clevers, E. J. P. de Koning, A. van Oudenaarden, De novo prediction of stem cell identity using single-cell transcriptome data. *Cell Stem Cell* **19**, 266–277 (2016).

86. Y. Wang, R. Wang, S. Zhang, S. Song, C. Jiang, G. Han, M. Wang, J. Ajani, A. Futreal, L. Wang, iTALK: An R package to characterize and illustrate intercellular communication. *BioRxiv* , 507871 (2019).
87. H. Chen, L. Albergante, J. Y. Hsu, C. A. Lareau, G. Lo Bosco, J. Guan, S. Zhou, A. N. Gorban, D. E. Bauer, M. J. Aryee, D. M. Langenau, A. Zinovyev, J. D. Buenrostro, G.-C. Yuan, L. Pinello, Single-cell trajectories reconstruction, exploration and mapping of omics data with STREAM. *Nat. Commun.* **10**, 1903 (2019).
88. E. M. Pietras, R. Lakshminarasimhan, J.-M. Techner, S. Fong, J. Flach, M. Binnewies, E. Passegué, Re-entry into quiescence protects hematopoietic stem cells from the killing effect of chronic exposure to type I interferons. *J. Exp. Med.* **211**, 245–262 (2014).
89. N. An, Y. Kang, *In vivo* BrdU incorporation assay for Murine hematopioetic stem cells. *Bio Protoc.* **3**, e960 (2013).

Acknowledgments: We are grateful to M. Shvedunova for valuable support in editing the manuscript and for critical feedback. Our special thanks to E. Trompouki and N. Cabezas-Wallscheid for critical feedback on the manuscript. We thank G. V. Renschler and Y. Sun for discussing bioinformatic analysis. We thank T. Stehle, J. Falkenstein, and W. Stawiarski for genotyping the animals. In addition, we thank T. Stehle for translating the BrdU application into German. We thank all the Akhtar laboratory members for critical feedback. We thank A. Lenaerts for sharing aged wild-type animals. The MPI-IE core facilities for Imaging, Deep sequencing (especially for C. Bella), Bioinformatics (especially for W. Deboutte), Mouse, and Flow cytometry (especially S. Hobitz and K. Schuldes) have been invaluable for this project. We are also thankful to J. Seyfferth and H. Holz for technical help. **Funding:** This study was supported by the German Research Foundation (DFG) under Germany's Excellence Strategy (CIBSS–EXC-2189, project ID 390939984). This work was also supported by the German Research Foundation (DFG) under the CRC 992 (A02), CRC 1425 (P04), and CRC 1381 (B3) awarded to A.A. **Author contributions:** Conceptualization: C.P.R. and A.A. Methodology: C.P.R. Investigation and original draft: C.P.R. Final manuscript writing: C.P.R. and A.A. Supervision: A.A. **Competing interests:** The authors declare that they have no competing interests. **Data and materials availability:** All data needed to evaluate the conclusions in the paper are present in the paper and/or the Supplementary Materials. The accession number for the RNA-seq data reported in this paper is Gene Expression Omnibus (NCBI) GEO: GSE166475, and the ATAC-seq is reported in GSE166476.

Submitted 18 March 2021
Accepted 21 June 2021
Published 6 August 2021
10.1126/sciadv.abi5987

Citation: C. P. Rodrigues, A. Akhtar, Differential H4K16ac levels ensure a balance between quiescence and activation in hematopoietic stem cells. *Sci. Adv.* **7**, eabi5987 (2021).